# FINAL REPORT

## Phenomenology and Signal Processing for UXO/Clutter Discrimination

SERDP Project MM-1595

AUGUST 2009

Thomas Bell
**SAIC**

This document has been approved for public release.

Strategic Environmental Research and Development Program

This report was prepared under contract to the Department of Defense Strategic Environmental Research and Development Program (SERDP). The publication of this report does not indicate endorsement by the Department of Defense, nor should the contents be construed as reflecting the official policy or position of the Department of Defense. Reference herein to any specific commercial product, process, or service by trade name, trademark, manufacturer, or otherwise, does not necessarily constitute or imply its endorsement, recommendation, or favoring by the Department of Defense.

# Table of Contents

1. Introduction ..... 1
2. Multiaxis EMI Measurements of Clutter Items ..... 4
   2.1. Time Domain Signature Data Collection ..... 4
   2.2. Frequency Domain Signature Data Collection ..... 8
3. EMI Signature Parameterization ..... 11
   3.1. Dipole Inversion of the EMI Signature Data ..... 11
   3.2. Parametric Forms ..... 16
4. Parameter Regimes for Clutter Items ..... 23
   4.1. Net Polarizability ..... 23
   4.2. Decay Curve Parameters ..... 24
5. Position-Independent Processing of EMI data ..... 30
   5.1. Empirical Parameterization ..... 30
   5.2. Parameter Values ..... 31
   5.3. Parameter Trajectories ..... 32
   5.4. Polarizability Calculations ..... 34
6. Intermediate Time Response ..... 36
   6.1. Parametric Representation ..... 36
   6.2. Parameter Values ..... 37
   6.3. EM61 Survey Data ..... 38
7. Bulk Magnetization ..... 40
   7.1. Demagnetizing Factors ..... 40
   7.2. Magnetization Responses of Munitions and Clutter ..... 41
8. Conclusions and Recommendations ..... 43
9. References ..... 46
Appendix A Clutter Items with Slope-Curvature Response Parameters Disjoint from the Corresponding Parameters for Munitions Items ..... A1
Appendix B Clutter and Munitions Items from Aberdeen Test Site ..... B1

# Figures

Figure 1. Examples of clutter items in the signature library. ..... 5
Figure 2. (a) Schematic of MTADS/MM-0601 TEM array and (b) array on test stand. ..... 6
Figure 3. (a) Repeat measurements of 2" diameter steel sphere compared model response. (b) Sphere response measured under individual array elements. ..... 6
Figure 4. TEM response for the leftmost clutter item shown in the top row of Figure 1(f), measured by the core nine MTADS TEM array elements. ..... 7
Figure 5. (a) Test setup with boxed target below GEM. (b) GEM field lines and measurement locations for normal and oblique illumination of target. ..... 8
Figure 6. (a) Overplotted responses to coil with 1.42 kHz characteristic frequency (symbols) from 16 measurements during a five hour period compared with expected response (solid curves). (b) Response to a 2" diameter steel ball compared with expected response. ..... 9
Figure 7. GEM signature data for the same target as in Figure 4. ..... 10
Figure 8. Basic elements of EMI sensor response. ..... 11
Figure 9. The yaw, pitch, roll rotation sequence. ..... 14
Figure 10. Principal axis polarizabilities corresponding to data shown in Figure 4. ..... 15
Figure 11. (a) EMI response curves measured above a 4.2 inch mortar. (b) Principal axis polariabilities calculated by inverting the complete set of response curves. ..... 16

Figure 12. Comparison of quadrature response for a variety of compact steel targets with the magnetic surface mode function (20). ..... 18
Figure 13. Parameter fits to principal axis polarizabilities for the clutter item used in the examples in Figure 4 and Figure 10. ..... 20
Figure 14. Parameterization of time domain response for a bent over half shell. ..... 21
Figure 15. Parameterization of time domain response for one of the horse shoes recovered at Camp Sibert. ..... 22
Figure 16. Distribution of net polarizability for clutter items listed in Table 1 ..... 23
Figure 17. Breakdown of cultural clutter by site. ..... 24
Figure 18. Principal axis decay curves for different classes of clutter. ..... 25
Figure 19. Distribution of modal amplitudes for various clutter items compared with modal amplitudes for a 76 mm projectile. ..... 25
Figure 20. Color-coded examples of different clutter types. ..... 26
Figure 21. Surface and body mode time scale distributions for the various clutter items. ..... 26
Figure 22. (a) Surface mode time scales for 4:1 aspect ratio cylinders. (b) Body mode time scales *vs.* material thickness. ..... 27
Figure 23. Surface and body mode time scales for different clutter types. ..... 28
Figure 24. Surface and body mode time scales for cultural clutter compared with munitions items. ..... 29
Figure 25. (a) Pasion-Oldenburg model fit to the EMI response of a 4.2 inch mortar aligned transverse to the primary field. (b) Comparison between the two-component and Pasion-Oldenburg model fits to the 4.2 inch mortar response. ..... 30
Figure 26. Pasion-Oldenburg exponent $\gamma$ compared to the magnetic crossover time $\tau_M$ for model fits to EMI data collected above a 4.2 inch mortar and a 60 mm mortar. ..... 31
Figure 27. Pasion-Oldenburg power law ($\gamma$) and decay time ($\tau$) parameters for various munitions items. ..... 32
Figure 28. Pasion-Oldenburg power law ($\gamma$) and decay time ($\tau$) parameters for several types of clutter items. ..... 33
Figure 29. (a) Decay time ($\tau$) and power law ($\gamma$) parameters for the 4.2 inch mortar. The trajectory is calculated by fitting the Pasion- Oldenburg model to linear combinations of the principal axis polarizabilities. (b) Parameter trajectory corresponding to linear combinations of the principal axis polarizabilities for the 4.2 inch mortar compared with that for a 60 mm mortar. ..... 34
Figure 30. Normalized polarizabilities for a 4.2 inch mortar (left) and a 60 mm mortar (right) calculated by conventional EMI inversion (blue) and by fitting parameter trajectories to unmapped EM data (red). ..... 35
Figure 31. Measured transverse 4.2 inch mortar response at EM61 time gates (symbols) and quadratic fit to the measured response (curve). ..... 36
Figure 32. Distribution of slope and curvature parameters for (a) projectiles, mortars and rockets and (b) submunitions and grenades. ..... 37
Figure 33. Slope and curvature parameters for various classes of clutter items. ..... 38
Figure 34. Shaw EM61 system at Aberdeen Proving Ground Standardized Test Site. ..... 38
Figure 35. Distributions of EM61 response slope and curvature for (a) APG munitions and (b) clutter items. ..... 39
Figure 36. (a) Demagnetizing factors for cylinders (solid lines) and ellipsoids (dashed lines) *vs.* length to diameter aspect ratio. Symbols are measured values for steel cylinders. (b) Effect of applied field direction on the demagnetizing factors for cylinders. ..... 41
Figure 37. Demagnetizing factors for munitions and clutter items. ..... 42

# Tables

Table 1. Breakdown of clutter items measured with the MTADS/MM-0601 TEM array. .....7

# Acronyms

| | |
|---|---|
| APG | Aberdeen Proving Ground |
| BUD | Berkeley UXO Discriminator |
| DARPA | Defense Advanced Research Projects Agency |
| EMI | Electromagnetic Induction |
| ESTCP | Environmental Security Technology Certification Program |
| LSBP | Lake Success Business Park redevelopment project |
| MTADS | Multi-sensor Towed Array Detection System |
| NRL | Naval Research Laboratory |
| Rx | Receive coil in EMI sensor |
| SERDP | Strategic Environmental Research and Development Program |
| TEM | Transient or Time Domain Electromagnetic Induction |
| Tx | Transmit coil in EMI sensor |
| UXO | Unexploded Ordnance |

# 1. Introduction

There are two basic parts to the process of discriminating between buried unexploded ordnance (UXO) and non-hazardous metallic clutter in the ground. First, target parameters or features are extracted from data collected over the target. Then the target parameters are supplied to a set of decision rules that classify the target as UXO or clutter. Despite significant investments from SERDP and ESTCP, UXO/clutter discrimination performance to date has not lived up to expectations. There are problems with both parts of the process. First, current discrimination techniques rely on inverting spatially mapped electromagnetic induction (EMI) data to estimate target parameters and are extremely sensitive to noise and small errors in data mapping. Second, discrimination performance depends crucially on the training data used in determining the boundaries of the decision regions. Although an extensive data base of UXO signatures has been compiled under SERDP project MM-1313 (Quantification of UXO variability for target discrimination), there is precious little clutter data collected under controlled conditions available for training.

The project was intended to help rectify this deficiency by collecting and analyzing EMI data for a variety of clutter items. Specific objectives were to (a) establish relationships between the parameters that characterize a target's EMI signature and the physical attributes of the target that can be used to develop effective classification rules and (b) devise robust processing and analysis procedures for estimating the target parameters from data collected above an unknown target without having to spatially map the data.

The first task was to acquire a database of EMI clutter signatures that could be used with the existing UXO signature database in developing and training new classification and discrimination algorithms. Work on this task is summarized in §2. An inventory of over 1000 clutter items recovered from various UXO sites has been assembled. It includes exploded ordnance fragments from the Badlands Bombing Range in Pine Ridge, South Dakota, cultural clutter items recovered from the Lake Success redevelopment project in Bridgeport, Connecticut (former Remington Arms site), range scrap recovered from Fort A.P. Hill as part of the DARPA backgrounds study [1, 2] and a variety of exploded ordnance fragments, range scrap and cultural clutter recovered from Camp Sibert in Alabama as part of the first ESTCP Discrimination Study. Time domain signature data for most of these objects were collected using the NRL MM-0601 transient EMI array (MTADS TEM array). Frequency domain signature data were collected using the Geophex GEM-3 sensor for a representative sample of the clutter items.

The second task was to extract relevant target parameters from the clutter signatures. There are two parts to the EMI response: magnetization of the object by the primary field transmitted by the sensor and the evolution of eddy currents set up in the object by changes in the primary field. The latter effect is present in both time and frequency domain data, while the magnetization effect is present only in the frequency domain data. We used the time domain data to parameterize the EMI response associated with the eddy current decay. The process is described in §3. First, the TEM array data are inverted to determine principal axis polarizabilities for each target, and then the principal axis polarizabilities are parameterized using a physics-based model that pairs an algebraic form for the early time response with an exponential decay for the late time response. Parameterization of the magnetization response using frequency domain data is described in §7.

Section 4 summarizes our work on how target parameters determined from two-component algebraic/exponential model fits to the signature data vary among different types of clutter and how they differ from corresponding parameters for munitions items. The results have important implications for the process of associating parameter values or features which characterize the polarizabilities with physical attributes or properties of the corresponding munitions or clutter items, and identifying regions of parameter space which correspond to different classes of munitions or clutter items.

In §§5 and 6 we examine the dependence of the target parameters on sensor/target orientation with the goal of determining the extent to which representative target parameters can be determined directly from data collected over a target without resorting to spatial mapping and dipole inversion. The goal here is to develop procedures for estimating target parameters that do not rely on spatially mapped data. We call this position-independent processing. Position-independent processing is amplitude-independent processing. We use only the shapes of the responses observed at various locations above the object, and do not particularly care where the measurements were taken. The approach is based on EMI signal attributes determined from simple parametric representations for the EMI signals measured above typical UXO or clutter items and how these parameters vary as the sensor is moved about over the item.

The analysis in §5 uses the full decay range of 0.04 msec to 25 msec. As a matter of convenience we represent the signatures using a simple three-parameter model described by Pasion and Oldenburg that combines the algebraic and exponential characteristics of the EMI response. The model is simpler than the complete two-component response model and can be used to adequately represent the response for all but the earliest part of the eddy current decay. The distributions of the power law and exponential decay parameter values for various classes of clutter items are found to be quite different from those of different munitions items. The trajectories of these parameter values that are swept out as a sensor is moved about over a munitions item are quite distinctive, and a simple procedure is introduced for estimating the shapes of the principal axis polarizability curves for munitions items from data collected as a sensor is blindly moved about over the item.

In §6 we restrict attention to the response over a limited range of decay times corresponding to the range sampled by the Geonics EM61 sensor, *viz.* 0.2 msec to 1.2 msec. Since this decay range does not extend far enough to sample the exponential regime for many items of interest, we use a simple model that is quadratic in log(signal) *vs.* log(time) to fit the data. The two shape parameters (slope and curvature in log space) then correspond to the average power law over the measurement range and how much it changes over the range. The parameter distributions for munitions and clutter have some similarity to the distributions of the power law and exponential decay rate parameters from §5, and it appears that some measure of position-independent classification should be possible even when the response is sampled over this restricted range.

We look at some EM61 survey data collected at the Aberdeen UXO Demonstration Site at the end of §6. The parameter distributions are somewhat more diffuse than were obtained using the MTADS TEM array data, but still seem to offer some UXO/clutter classification potential. Specifically, in cases where EM61 survey data is used to detect targets for later classification using cued systems, it may be possible to identify some high confidence clutter items directly from the EM61 survey data and thereby reduce the number of cued data collections that have to be done.

We shift attention to the frequency domain response in §7. There are two basic components in the EMI response to munitions and clutter items: magnetization of the object by the primary field

transmitted by the sensor and the evolution of eddy currents set up in the object by changes in the primary field. The results reported in §§3-6 deal with the eddy current response, which does not exploit all of the information that is available in the EMI response. §7 deals with that part of the EMI response that is associated with bulk magnetization of the target. An object's shape affects how it responds to magnetic fields. The effects are represented by demagnetizing factors that depend on the direction of the applied field relative to the object and are determined by the physical details of how the object responds to externally applied magnetic fields. These demagnetizing factors are another amplitude-independent response parameter and can be determined by fitting the in-phase part of the frequency domain response data with a simple model. Distributions of the demagnetizing factors for munitions and clutter items are distinctly different. This reflects very real shape differences. The munitions items are basically 4:1 aspect ratio cylinders as far as the magnetization response is concerned, and their demagnetizing factors cluster accordingly. Values for the clutter items scatter over a much wider range, and the maximum demagnetizing factors for the clutter items are often significantly larger than for the munitions. These are consequences of the facts that the clutter items tend to be irregularly shaped and that many of them have one dimension significantly smaller than the other two.

A brief summary is given in §8. Appendices A and B include pictures of representative clutter items that have signature parameters that are significantly different than those of UXO items.

## 2. Multiaxis EMI Measurements of Clutter Items

The first task of this project was to assemble a clutter signature library based on multiaxis EMI measurements of clutter items. An inventory of over 1000 clutter items recovered from various cleanup sites has been assembled. The clutter items include exploded ordnance fragments from the Badlands Bombing Range in Pine Ridge, South Dakota, cultural clutter items recovered from the Lake Success redevelopment project in Bridgeport, Connecticut (former Remington Arms site), range scrap recovered from Fort A.P. Hill as part of the DARPA backgrounds study [1, 2] and a variety of exploded ordnance fragments, range scrap and cultural clutter recovered from Camp Sibert in Alabama as part of the first ESTCP Discrimination Study. Figure 1 shows some examples of the clutter items in the library. The items in Figure 1(a) are smaller clutter from Fort A.P. Hill and the former Remington Arms plant at Bridgeport, Connecticut. They include ordnance related clutter (spent 50 caliber rounds, M82 7.62mm blank cartridges and cartridge clips), metal scraps and wire, and cultural clutter items. Note the 12 inch ruler. It is included for scale in the other pictures. Figure 1(b) shows 4.2 inch mortar nose frag and base plates recovered from Camp Sibert. Some of the smaller frag items from Camp Sibert are shown in Figure 1(c). Typical agricultural, industrial and other clutter items of cultural origin are shown in Figure 1(d). These items came from Camp Sibert and the former Remington Arms site. They include broken pieces of plows and other implements, hand tools, and especially horse/mule shoes and broken pieces of shoes. Figure 1(e) shows exploded ordnance fragments from the Badlands Bombing Range, while Figure 1(f) shows larger clutter items from Fort A.P. Hill, Camp Sibert, and the former Remington Arms site.

Both time and frequency domain signature data were acquired. Time domain signature data were collected for the entire library using the MTADS TEM array designed and built for ESTCP Project MM-0601 by G&G Sciences of Grand Junction, Colorado [3, 4]. The sensor array and data collection procedures are described in §2.1 below. Frequency domain data were collected using a Geophex GEM-3 sensor [5] as described in §2.2 below. This process was considerably more labor intensive, and consequently only a representative subset of the library items were measured. As described in Ch. 7, some of the information in the two types of measurement is redundant. Our analysis of the frequency domain data focuses on the unique contributions from the frequency domain, which relate to magnetization effects in the EMI response.

### 2.1. Time Domain Signature Data Collection

The MTADS/MM-0601 TEM array that was used to acquire time domain clutter signatures consists of a square array of 25 Tx/Rx pairs, shown schematically in Figure 2(a). The Tx/Rx pairs consist of concentric 35 cm square transmit coils (shown in red in the drawing) and 25 cm square receive coils (shown in blue). For the clutter signature data, the time domain response was measured from 0.04 msec to 25 msec after the primary field cutoff using the central core of 9 transmitters and all 25 receivers. Figure 2(b) shows the array on the test stand used for the time domain clutter signature measurements. The test stand was set up in the MTADS garage at NRL's Blossom Point site [6].

Extensive testing of the array sensors in MM-0601 has shown them to be very accurate, stable and reliable. Figure 3(a) shows 24 repeat measurements (plotted in red) of a 2 inch diameter carbon steel sphere at intervals of 125 sec, for a total duration of 48 min. The data were collected outside in an open environment with the prototype MM-0601 Tx/Rx coil pair at Grand Junction,

Colorado in January 2007. The sphere was 30 cm from the base of the Tx/Rx pair, on the coil axis. With this test setup the target signal was very strong compared to background levels, and the plotted response curves do not have the background subtracted. They are normalized by the transmitter current. The dashed line shows a fit of the data to the expected TEM response for a permeable sphere [7], using a conductivity of $3.2\times10^6$ S/m and a relative permeability of 62.5, values which are within the expected range for carbon steel [8]. Figure 3(b) shows data on the same sphere collected with the final array at Blossom Point in August 2007. In this case, the sphere was suspended 25 cm below each of the array Tx/Rx pairs in turn. The red lines show the

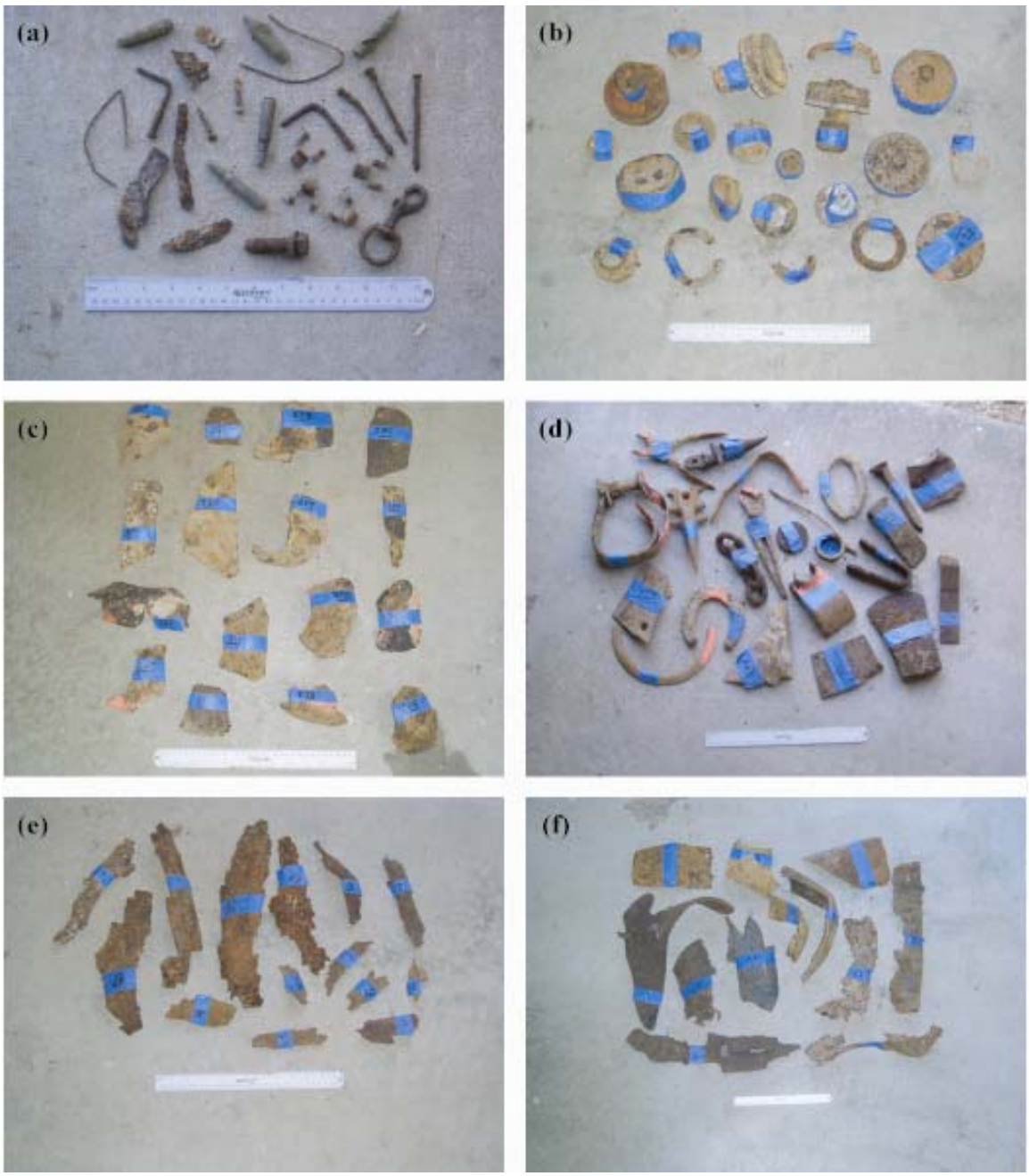


**Figure 1. Examples of clutter items in the signature library.**

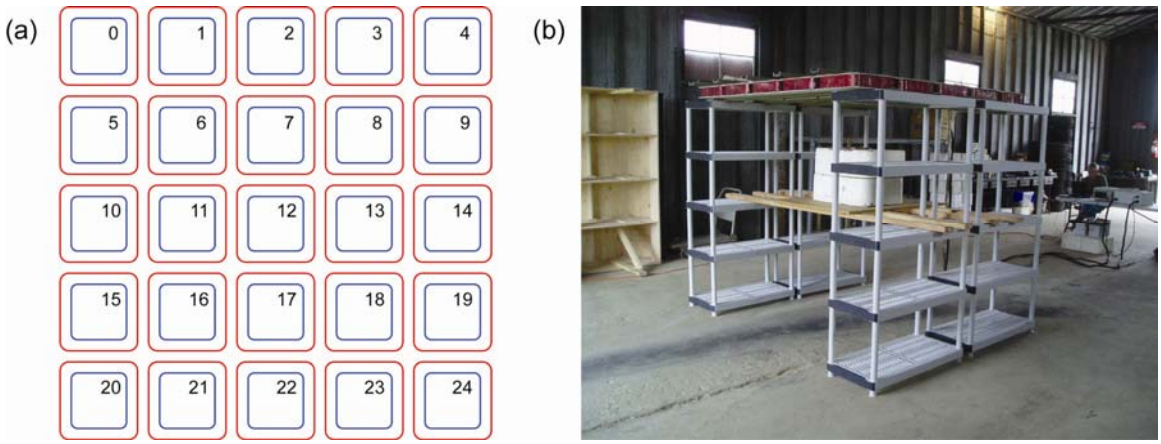


**Figure 2. (a) Schematic of MTADS/MM-0601 TEM array and (b) array on test stand.**

individual responses. The dashed line shows the expected sphere response. The apparent inconsistencies in noise levels and signal strength between Figure 3(a) and Figure 3(b) are due to the fact that between January 2007 and delivery of the array to Blossom Point the coils were redesigned to reduce weight and the amplifier gains were modified.

Signature data on 996 clutter items were collected with the MTADS TEM array. Table 1 gives a summary breakdown. The items referred to as "half shells" are what is produced when the cylindrical body of a 4.2 inch mortar is blown open flat. Each clutter item was set below the array, more or less centered under array element 12. Distance below the array varied with the size of the target, and was chosen to give a subjectively good signal level. Figure 4 is an example of the data collected using the MTADS TEM array. It shows signals *vs.* decay time (time after primary field cutoff) measured with the core nine Tx/Rx pairs (array elements 6, 7, 8, 11, 12, 13, 16, 17 and 18) for one of the half shells from Camp Sibert. This clutter item is the leftmost object in the top row of Figure 1(f). The complete set of data includes measured responses from all of the receivers for each transmit pulse, not just the receiver co-located with the transmitter.

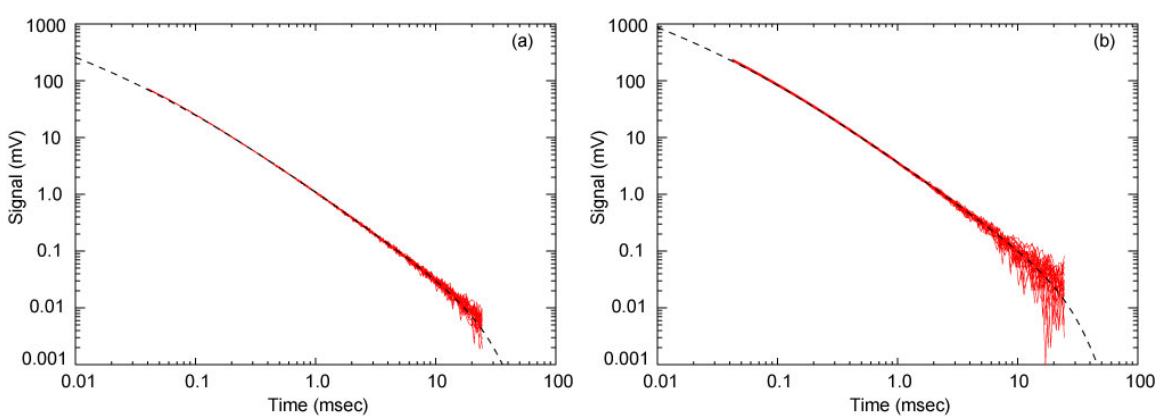


**Figure 3. (a) Repeat measurements of 2" diameter steel sphere compared model response. (b) Sphere response measured under individual array elements.**

| | | |
|---|---|---|
| Camp Sibert | Half-shell | 63 |
| | Base plate | 91 |
| | Nose frag. | 97 |
| | Misc. frag & cultural | 552 |
| | Total | 803 |
| Other Sites* | | 193 |
| Total | | 996 |

* Fort A.P. Hill (range scrap), Badlands Bombing Range (frag), former Remington Arms plant (cultural)

**Table 1. Breakdown of clutter items measured with the MTADS/MM-0601 TEM array.**

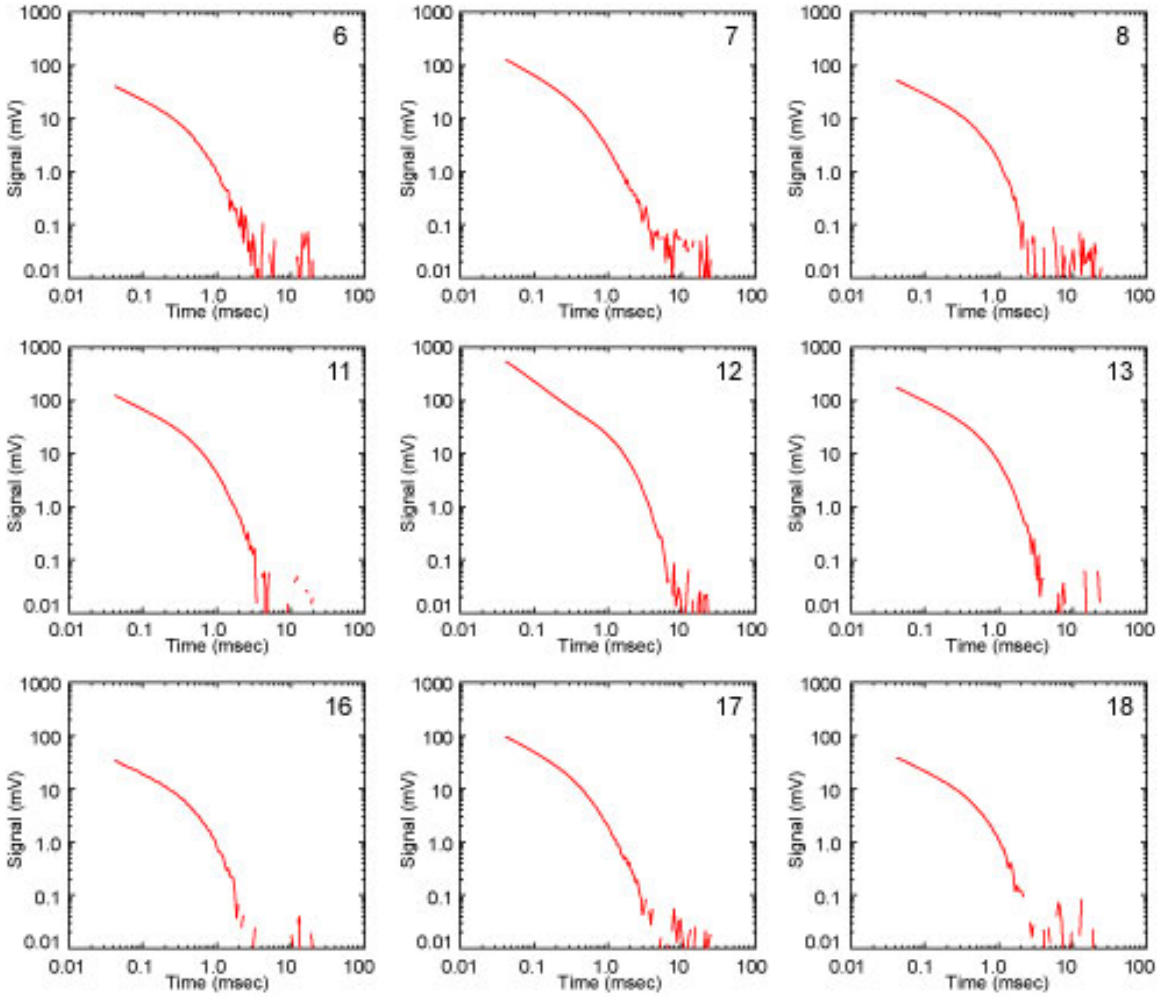


**Figure 4. TEM response for the leftmost clutter item shown in the top row of Figure 1(f), measured by the core nine MTADS TEM array elements.**

## 2.2. Frequency Domain Signature Data Collection

Frequency domain clutter signature data were collected using a Geophex GEM-3 sensor. The sensor has a 40 cm diameter primary transmit coil concentric to a 23 cm diameter bucking coil. These coils are concentric to a 12.1 cm receive coil. The primary field includes the combined effects of the transmit and bucking coils, which are designed to cancel the net flux through the receive coil [5]. Measurements were taken at ten logarithmically spaced frequencies over a range extending from 90 Hz to 50 kHz.

For the frequency domain measurements each clutter item was secured in a box (*e.g.*, with cable ties) which is then set on a board below the GEM-3 as shown in Figure 5(a). Different size boxes were used to accommodate different size clutter items. Data were collected with each of the six faces of the box pointing up in turn, first with the box directly below the sensor (location A) and then with the box off to the side in one of two locations (B or C) for oblique illumination. Figure 5(b) shows the field lines at the box for location A (directly under the coil) and location B, which is 25 cm from the coil centerline. Location C is 43 cm from the coil centerline. Figure 5(a) shows the box in location C. A different board with different geometry was used to accommodate larger targets. The idea was to illuminate the box and its target from a full complement of orthogonal and oblique angles in order to gather enough data to determine the target's principal axes and corresponding polarizabilities. Measurements through opposite faces of the box help in determining the actual location of the target dipole within the box. We chose this procedure rather than collecting data on a regular grid below the sensor because it seemed to be more efficient. GEM background levels tend to drift around on time scales comparable to representative data collection time scales (a few to fifteen or more minutes). By systematically varying the target orientation relative to the primary field, we can get by with fewer measurements (16 *vs.* the typical 25 or more for grid measurements).

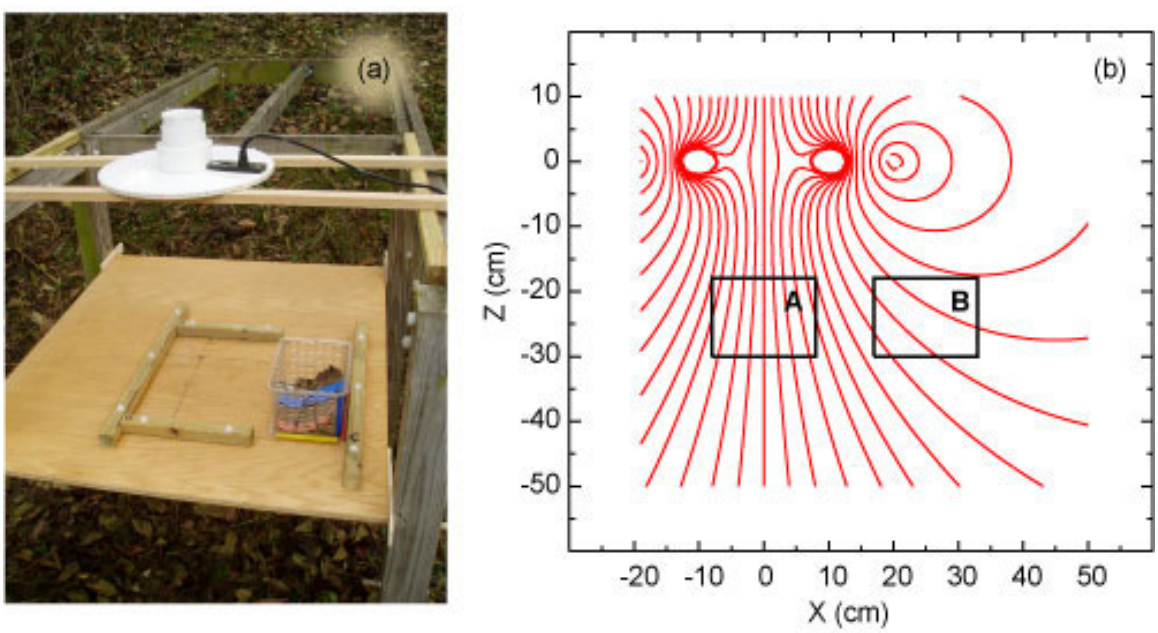


**Figure 5. (a) Test setup with boxed target below GEM. (b) GEM field lines and measurement locations for normal and oblique illumination of target.**

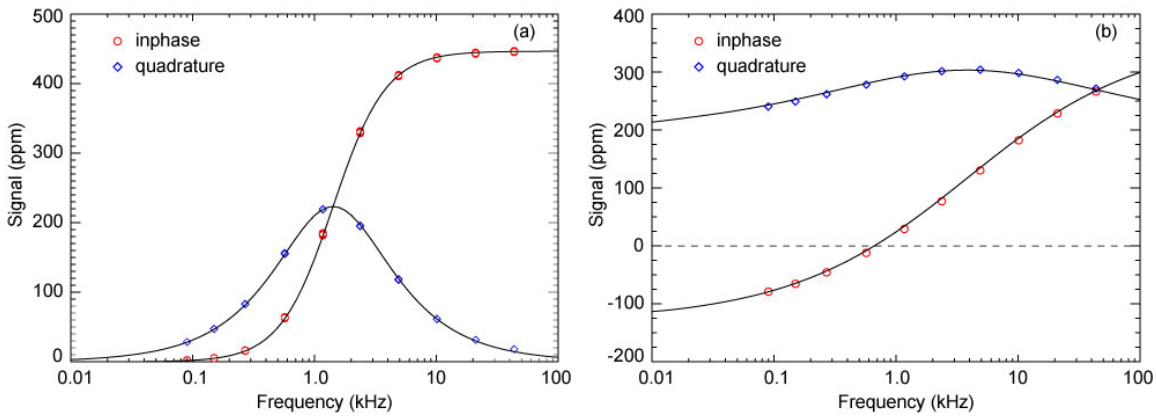


**Figure 6. (a) Overplotted responses to coil with 1.42 kHz characteristic frequency (symbols) from 16 measurements during a five hour period compared with expected response (solid curves). (b) Response to a 2" diameter steel ball compared with expected response.**

The GEM background levels were monitored during the measurement sequence and subtracted from the signature measurements. Every measurement is a roughly ten second average of the GEM signal, and every fourth measurement is a blank background. In order to monitor the GEM calibration, each data sequence started with a measurement of the responses to a ferrite rod and a small coil with a characteristic frequency of 1.42 kHz. The ferrite response should be exactly 180° out of phase with the primary field, and constant over frequency. We typically find that the phase shift varies by no more than a few tenths of a degree over the frequency range, and that the amplitude is flat to within about one percent. Coil responses in phase with the primary field and 90° out of phase (in quadrature) with the primary field are shown in Figure 6(a). Sixteen measurements taken over a five hour period are overplotted. The red circles are the measured in-phase response and the blue diamonds are the measured quadrature response. The solid curves show the expected response for the coil. Figure 6(b) shows the measured response for the 2 inch steel ball whose time domain response is shown in Figure 3. The curves show the calculated frequency domain response [9] using the same parameter values as before ($\sigma = 3.2\times10^6$ S/m, $\mu_R = 62.5$).

Signature data collection using this procedure takes substantially more time than using the TEM array to collect time domain data. Consequently, only a representative sample of 122 of the clutter items was measured with the GEM. Figure 7 shows an example of the GEM signature data. The target is the half shell used to illustrate the time domain signature data in Figure 4. The in-phase responses are shown in red, quadrature in blue. Each plot is for a different location/orientation combination. Locations are identified by a letter (A or C in this case), and orientations by axis color and direction. For example, "A-Blu-Up" means that the box is set on the board at location A with the blue axis pointing up. This is the geometry shown in Figure 5(a). For the measurements shown in Figure 7, the board is 50 cm below the sensor. The box axes are color coded blue, red and yellow to avoid confusion in placing the box in the right orientation. Location A is directly under the sensor, while C is 43 cm off to the side.

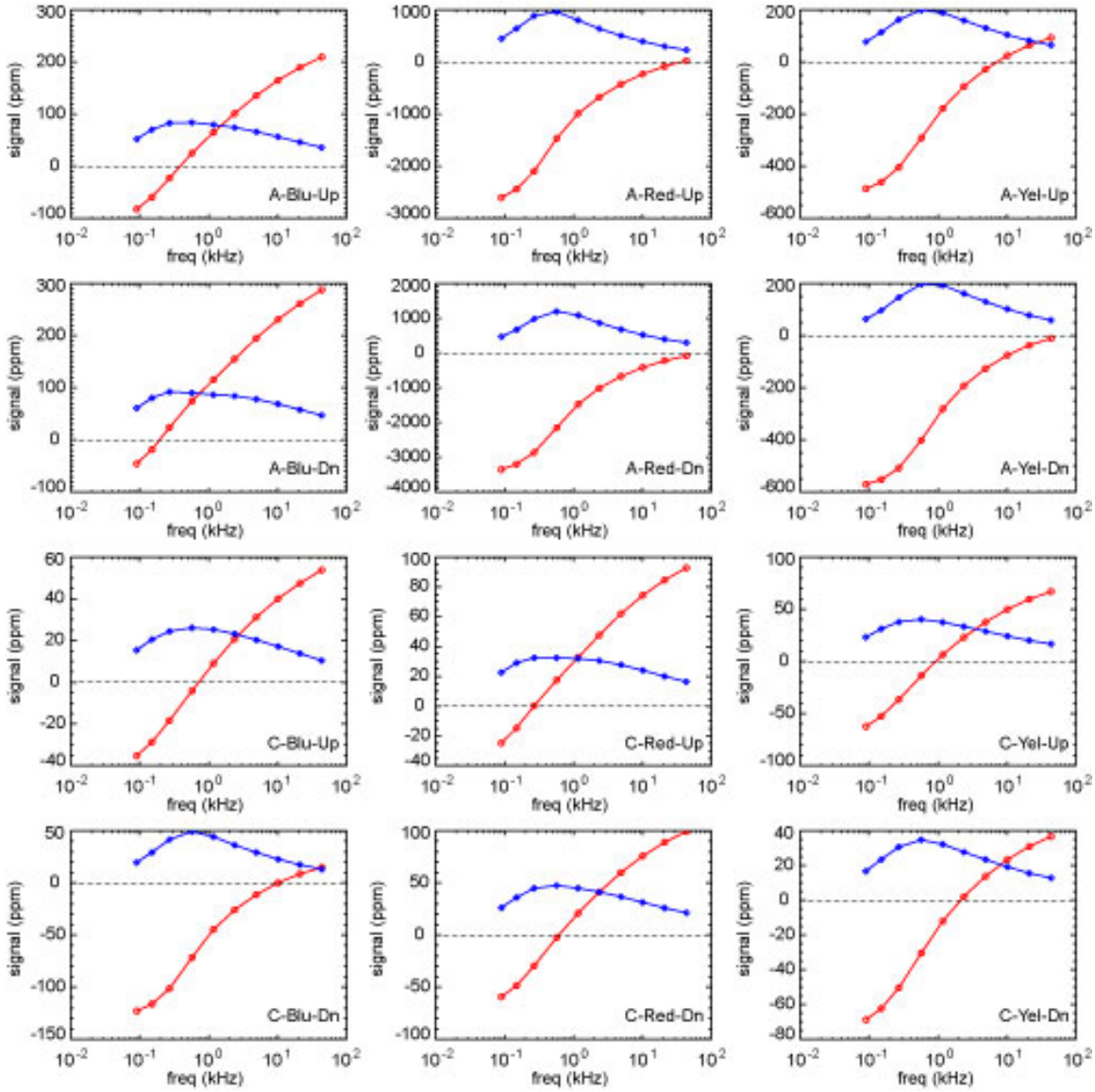


**Figure 7. GEM signature data for the same target as in Figure 4.**

## 3. EMI Signature Parameterization

While useful in their own right, the raw signature data reflect details of the sensor/target geometry as well as inherent EMI response characteristics of the targets themselves. In order to separate out the intrinsic target response properties from sensor/target geometry effects we invert the signature data to estimate principal axis magnetic polarizabilities for the targets. As described in §3.1 below, the clutter signature data are inverted using the standard induced dipole response model wherein the effect of eddy currents set up in the target by the primary field is represented by a set of three orthogonal magnetic dipoles at the target location [10, 11]. Parametric representations for the principal axis polarizability curves are described in §3.2.

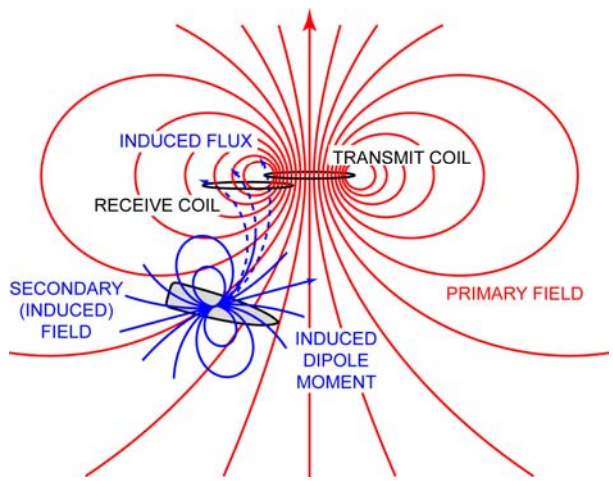


**Figure 8. Basic elements of EMI sensor response.**

### 3.1. Dipole Inversion of the EMI Signature Data

Figure 8 illustrates the basic elements of the EMI process. The primary field $\mathbf{H}_0$ is produced by current flowing in the transmit coil. The relationship between the primary field and the transmit current I can be expressed in terms of a transmit coil sensitivity function $\mathbf{C}_T$ such that

$$\mathbf{H}_0 = n_T \mathbf{C}_T I . \tag{1}$$

We have explicitly pulled out the number of turns in the coil $n_T$ in order that the sensitivity function can be calculated as an integral around a single loop of the transmit coil using the Biot-Savart law,

$$\mathbf{C}_T(\mathbf{r}) = \frac{1}{4\pi} \oint \frac{d\mathbf{l}_T \times (\mathbf{r} - \mathbf{r}_T)}{|\mathbf{r} - \mathbf{r}_T|^3} . \tag{2}$$

Here $\mathbf{r} - \mathbf{r}_T$ is a vector from a point on the coil $\mathbf{r}_T$ to the field point $\mathbf{r}$. Changes in the primary field $\mathbf{H}_0$ induce eddy currents in the target, which in turn produce the induced field $\mathbf{H}_I$. The signal S(t) is proportional to the receiver voltage V(t) created by a changing magnetic flux through the coil due to $\mathbf{H}_I$ (Faraday's law):

$$S(t) \propto V(t) = -\frac{d}{dt}\int \mathbf{B}_I \cdot d\mathbf{a}_R \ . \tag{3}$$

In equation (3) the magnetic induction or flux density $\mathbf{B}_I = \mu_0\mathbf{H}_I$. Stokes' theorem can be used to relate the integral of the flux density $\mathbf{B}$ ($= \nabla \times \mathbf{A}$) over a surface enclosed by a loop to an integral around the loop of the corresponding vector potential $\mathbf{A}$, so that

$$V(t) = -\frac{d}{dt}\oint \mathbf{A}_I \cdot d\mathbf{l}_R \ . \tag{4}$$

We represent the effect of the eddy currents in the target by an induced dipole moment $\mathbf{m}$, which is related to the primary field according to

$$\mathbf{m}(t) = \int \mathbf{H}_0(\tau)\mathbf{B}(t-\tau)d\tau \ . \tag{5}$$

In equation (5), $\mathbf{B}$ is the magnetic polarizability tensor. It completely describes the induced dipole response of the target. The eigenvalues of $\mathbf{B}$ correspond to responses induced by field components aligned with each of the target's principal axes. For a frequency-domain EMI system with $\mathbf{H}_0(t)=\mathbf{H}_0\exp(i\omega t)$,

$$\begin{aligned}\mathbf{m}(t) &= \int \mathbf{H}_0 \exp(i\omega t)\mathbf{B}(t-\tau)d\tau \\ &= \mathbf{H}_0 \exp(i\omega t)\hat{\mathbf{B}}(\omega)\end{aligned} \tag{6}$$

where $\hat{\mathbf{B}}(\omega)$ is the Fourier transform of $\mathbf{B}(t)$:

$$\hat{\mathbf{B}}(\omega) = \int \mathbf{B}(t)\exp(-i\omega t)dt \ . \tag{7}$$

The vector potential at a field point $\mathbf{r}$ due to the induced dipole moment $\mathbf{m}$ in an object at position $\mathbf{r}_0$ is given by

$$\mathbf{A}_I = \frac{\mu_0}{4\pi}\frac{\mathbf{m}\times(\mathbf{r}-\mathbf{r}_0)}{|\mathbf{r}-\mathbf{r}_0|^3} \ . \tag{8}$$

The receiver voltage is then

$$V(t) = -\frac{d}{dt}\frac{\mu_0}{4\pi}\oint \frac{(\mathbf{m}\times(\mathbf{r}_R - \mathbf{r}_0))\cdot d\mathbf{l}_R}{|\mathbf{r}_R - \mathbf{r}_0|^3}\,. \tag{9}$$

Since the scalar triple product $(\mathbf{m}\times\mathbf{r})\cdot d\mathbf{l} = \mathbf{m}\cdot(\mathbf{r}\times d\mathbf{l}) = \mathbf{m}\cdot(d\mathbf{l}\times(-\mathbf{r}))$, this is equivalent to

$$\begin{aligned} V(t) &= -\left(\frac{\mu_0}{4\pi}\oint \frac{d\mathbf{l}_R \times (\mathbf{r}_0 - \mathbf{r}_R)}{|\mathbf{r}_0 - \mathbf{r}_R|^3}\right)\cdot\frac{d\mathbf{m}}{dt} \\ &= -\mu_0 n_R \mathbf{C}_R \cdot \frac{d\mathbf{m}}{dt} \end{aligned} \tag{10}$$

Where now $\mathbf{C}_R$ is the receiver coil sensitivity function and $n_R$ is the number of turns in that coil. Inserting the expressions for the induced dipole moment and the primary field from equations (5) and (1), respectively, we have

$$V(t) = -\mu_0 n_R n_T \mathbf{C}_R(\mathbf{r}_0 - \mathbf{r}_R)\cdot\mathbf{C}_T(\mathbf{r}_0 - \mathbf{r}_T)\int I'(t-\tau)\mathbf{B}(\tau)d\tau\,. \tag{11}$$

For an ideal time-domain sensor (current maintained at a constant level $I_0$ and then instantaneously returned to zero), this becomes

$$V(t) = \mu_0 n_R n_T I_0 \mathbf{C}_R \cdot \mathbf{C}_T \mathbf{B}(t)\,. \tag{12}$$

Alternatively, for an ideal frequency-domain measurement with $I(t) = I_0\exp(i\omega t)$,

$$V(t) = -i\omega\mu_0 n_R n_T I_0 \mathbf{C}_R \cdot \mathbf{C}_T \hat{\mathbf{B}}(\omega)\exp(i\omega t)\,. \tag{13}$$

In the coordinate frame defined by the principal axes of the target,

$$\mathbf{B}(t) = \begin{bmatrix} \beta_1(t) & 0 & 0 \\ 0 & \beta_2(t) & 0 \\ 0 & 0 & \beta_3(t) \end{bmatrix} \tag{14}$$

where $\beta_i(t)$ are the eigenvalues of the polarizability tensor $\mathbf{B}(t)$.

The target orientation is specified by an ordered sequence of three plane rotations of the principal axes involving the Euler angles $\psi$, $\theta$ and $\phi$ (yaw, pitch and roll, respectively). This is illustrated in Figure 9. In general, for a target with orientation $\psi$, $\theta$, $\phi$ the polarizability tensor can be expressed in terms of the action of a rotation matrix $\mathbf{U}$,

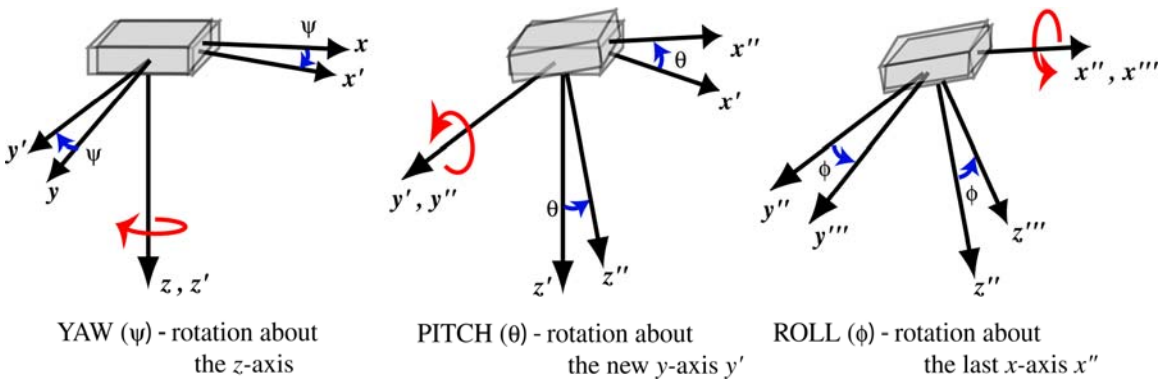


**Figure 9. The yaw, pitch, roll rotation sequence.**

$$\mathbf{U} = \begin{bmatrix} \cos\psi\cos\theta & \sin\psi\cos\theta & -\sin\theta \\ -\sin\psi\cos\phi + \cos\psi\sin\theta\sin\phi & \cos\psi\cos\phi + \sin\psi\sin\theta\sin\phi & \cos\theta\sin\phi \\ \sin\psi\sin\phi + \cos\psi\sin\theta\cos\phi & -\cos\psi\sin\phi + \sin\psi\sin\theta\cos\phi & \cos\theta\cos\phi \end{bmatrix} \tag{15}$$

on the principal axis (diagonal) form of **B** in (14):

$$\mathbf{B}(t) = \mathbf{U}\begin{bmatrix} \beta_1(t) & 0 & 0 \\ 0 & \beta_2(t) & 0 \\ 0 & 0 & \beta_3(t) \end{bmatrix}\mathbf{U}^{\mathbf{T}} \tag{16}$$

with the inverse of the rotation matrix being given by its transpose $\mathbf{U}^{\mathbf{T}}$.

Equations (11)-(13) each include three basic terms:

1. A normalization factor $\mu_0 n_R n_T I_0$, with or without the $i\omega$, that depends only on the transmit and receive electronics,

2. The coil sensitivity functions $\mathbf{C}_R$ and $\mathbf{C}_T$ that depend only on geometry and the target location relative to the sensor, and

3. The polarizability tensor $\mathbf{B}(t)$, or its Fourier transform $\hat{\mathbf{B}}(\omega)$, which specifies the intrinsic properties of the target (βs) and its orientation.

Given a set of measurements of the target response with varying geometries or "look angles" such that the corresponding coil response functions $\mathbf{C}_T$ and $\mathbf{C}_R$ cover a full range of directions at the target, the data can be inverted to determine the (X, Y, Z) location of the target, the orientation of its principal axes (ψ, θ, ϕ), and the principal axis polarizabilities ($\beta_1$, $\beta_2$, $\beta_3$). The basic idea is to search out the set of six parameters (X, Y, Z, ψ, θ, ϕ) and three functions ($\beta_1$, $\beta_2$, $\beta_3$) that minimizes the difference between the measured responses and those calculated using the appropriate one of equations (11)-(13). With some variations in the details, this approach has

been used by a number of research groups in developing procedures to classify buried objects on the basis of their EMI response [12, 13, 14, 15, 16, 17].

For the MTADS TEM array data, inversion is accomplished by a two-stage method. In the first stage, the target's (X, Y, Z) dipole location beneath is solved for non-linearly. At each iteration within this inversion, the nine element polarizability tensor (**B**) is solved linearly. We require that this tensor be symmetric; therefore, only six elements are unique. Initial guesses for X and Y are determined by a signal-weighted mean. The routine loops over a number of initial guesses in Z, keeping the result giving the best fit as measured by the chi-squared value. The non-linear inversion is done simultaneously over all time gates, such that the dipole (X, Y, Z) location applies to all decay times. At each time gate, the eigenvalues and angles are extracted from the polarizability tensor.

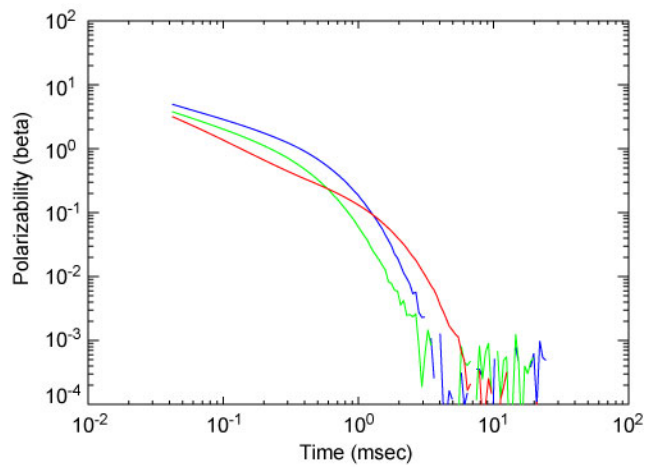


**Figure 10. Principal axis polarizabilities corresponding to data shown in Figure 4.**

In the second stage, six parameters are used: the three spatial parameters (X, Y, Z) and three angles representing the yaw, pitch, and roll of the target (Euler angles $\psi$, $\theta$, $\phi$). Here the eigenvalues of the polarizability tensor are solved for linearly within the 6-parameter non-linear inversion. In this second stage both the target location and its orientation are required to remain constant over all time gates, consistent with the basic dipole response construct [10]. The value of the best fit X, Y, and Z from the first stage, and the median value of the first-stage angles are used as an initial guess for this stage. Additional loops over depth and angles are included to better ensure finding the global minimum.

Figure 10 shows an example of the principal axis polarizabilities in the time domain. It corresponds to the MTADS TEM array data shown in Figure 4. The target, one of the Camp Sibert half shells, is a slightly bent plate about ¼ inches thick. The red curve is the polarizability when the primary field is normal to the surface of the plate, while the green and blue curves correspond to cases where the primary field is aligned along one of the edges. Figure 11 gives an example for a munitions item. Figure 11(a) shows EMI response curves measured with the TEM array 49 cm above a 4.2 inch mortar. (Only those response curves with a peak signal greater than 5 mV are plotted.) Figure 11(b) shows the principal axis polarizabilities calculated by inverting the complete set of TEM array data. Here, the red curve is the axial polarizability and the blue and green curves are transverse polarizabilities.

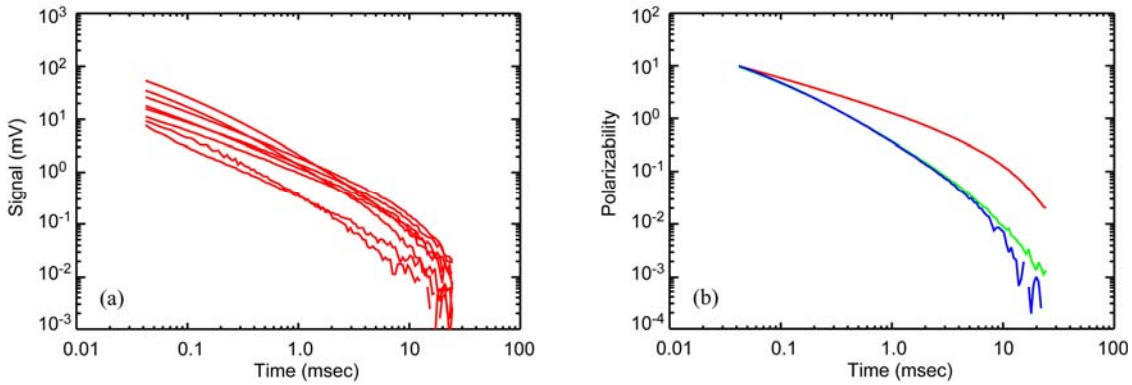


**Figure 11. (a) EMI response curves measured above a 4.2 inch mortar. (b) Principal axis polariabilities calculated by inverting the complete set of response curves.**

## 3.2. Parametric Forms

EMI response curves for compact metal objects such as UXO and much of the clutter do not typically have much structure, and can be represented using rather simple empirical expressions [13, 18]. Here, we explore an alternative parametric representation for the decay curves that is motivated by the basic physics of the EMI response.

With metal objects at typical EMI frequencies (<100 kHz), displacement currents associated with changing electric flux density can be neglected compared to conduction currents, and the EMI process is basically one of diffusion [10, 19]. The magnetic field inside the object obeys a vector diffusion equation

$$\frac{\partial \mathbf{H}}{\partial t} - \frac{1}{\sigma\mu}\nabla^2 \mathbf{H} = 0\,, \tag{17}$$

where $\sigma$ and $\mu$ are respectively the electrical conductivity and magnetic permeability of the object. We are primarily interested in objects having high relative permeability $\mu_R = \mu/\mu_0$, where $\mu_0 = 4\pi x10^{-7}$ H/m is the permeability of free space. The quantity $D = 1/\sigma\mu$ serves as the diffusion coefficient. As with other diffusion problems, the general EMI response when the object is placed in a magnetic field which is then suddenly removed can be expressed as a sum of modes whose amplitudes decay exponentially in time at rates that depend on the size, shape and composition of the object and on the spatial structure of the respective modes [10, 11, 20]. The more rapidly decaying modes correspond to proportionally smaller spatial scales of variation. The fundamental mode decays most slowly, and ultimately dominates the response. It decays on a time scale $\tau_0 \propto \sigma\mu L_0^2$, where $L_0$ is a characteristic length scale of the object. Consequently, we represent the late time response by

$$\beta_{\text{late}} = A_0 \exp(-t/\tau_0) \tag{18}$$

The initial response of an object in a magnetic field which is rapidly extinguished is governed by the dynamics of the screening currents which are set up on the surface of the object at the instant

the magnetic field is removed. At the outset as these currents start to diffuse into the object, $\partial \mathbf{H} / \partial t \sim t^{-1/2}$ [20, 21]. If the object is highly permeable ($\mu_R >> 1$), then this process is modified by the appearance of magnetic surface modes which eventually lead to a more rapid time decay with $\partial \mathbf{H} / \partial t \sim t^{-3/2}$ [22]. Weichman refers to the time scale that marks the transition between these two early time regimes as the magnetic crossover time, $\tau_M$. In the magnetic crossover transition zone, the magnetic surface modes produce fields that vary with time according to

$$-\frac{\partial \mathbf{H}}{\partial t} \sim \frac{1}{\sqrt{\pi t}} - \kappa e^{\kappa^2 t} \mathrm{erfc}(\kappa\sqrt{t}) \tag{19}$$

where *erfc*( ) is the complimentary error function and $\tau_M = 1/\kappa^2$ is the time scale for magnetic crossover.

Equation (19) describes exactly the early time response for a highly permeable sphere [23], which has only one characteristic length scale describing the surface curvature. The frequency dependence of the magnetic surface mode is given by the Fourier transform of the impulse response corresponding to equation (19). Hence in the magnetic crossover transition zone, the magnetic surface modes produce fields that, to within an additive constant, vary with frequency as

$$\mathbf{H}(\omega) \sim \frac{-1}{\kappa + (i\omega)^{1/2}} \tag{20}$$

[24]. The peak quadrature response occurs at $\omega = 2\pi f = \kappa^2$. Equation (20) has been found to provide a reasonably good representation of the response near the peak of the quadrature spectrum for a variety of compact steel objects [18]. This is illustrated in Figure 12, which is a composite of 58 measured quadrature spectra of compact steel targets, including a variety of inert ordnance items, plates, cylinders, I-beam pieces, *etc*. For each of the targets, the response was measured with the GEM-3 at frequencies of 30, 90, 210, 510, 1350, 3570, 9210, and 23970 Hz. The spectra are normalized to the quadrature peak. Individual data points correspond to values of the response normalized by the peak quadrature response for that target, with $\kappa^2$ equal to $2\pi$ times the frequency at which the quadrature peak occurs. The solid curve is $2(1+\sqrt{2})\kappa$ times the imaginary part of equation (20), which brings the amplitude of the surface mode function to unity at the peak at $\omega/\kappa^2 = 1$. For the most part the fit to the data is quite good.

In general, the magnetic surface mode response given by equation (19) applies locally in different areas of the surface, with the local $\tau_M$ depending on the surface curvature of the target in that area [22]. The sphere response follows equation (19) exactly in the magnetic crossover regime because there is only one characteristic length scale associated with the surface curvature. For a compact, but not spherical object we expect that the response in the crossover region will be somewhat distorted, although it should retain the asymptotic $t^{-1/2}$ and $t^{-3/2}$ limiting behavior. To accommodate this, we use a generalized parametric form

$$\beta_{early} = \frac{A_M}{(t/\tau_M)^{1/2}[1 + (t/\tau_M)^{\gamma}]^{1/\gamma}} \tag{21}$$

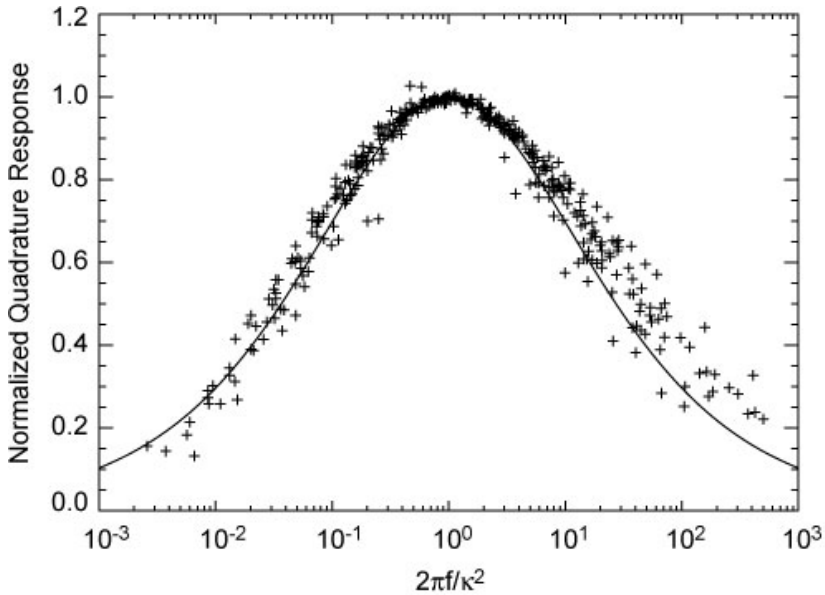


**Figure 12. Comparison of quadrature response for a variety of compact steel targets with the magnetic surface mode function (20).**

with an effective magnetic crossover time $\tau_M$ that corresponds to some composite of the surface mode transition over the entire object and a parameter $\gamma$ which controls the width of the magnetic crossover regime. A loosely similar modification of the width of the crossover regime in the equation (20) has been shown to give improved parametric representations of frequency domain responses of UXO and UXO-like objects [18]. Equation (21) does in fact faithfully reproduce the form of equation (19) to within a few percent over at least six decades of time using $\tau_M \cong 0.56/\kappa^2$ and $\gamma \cong 2/3$.

The principal axis polarizabilities for the time domain clutter data have been parameterized using equations (21) and (20) at early and late time, respectively. The algorithm for fitting these expressions to the principal axis decay curves starts out by fitting equation (21) to the response for $t \leq 0.1$ msec, and then increasing the time range until the measured response starts to diverge from the basic algebraic form represented by equation (21). The remainder of the response is then fit to an exponential form as in equation (20). This proceeds by first identifying a few msec stretch of the late lime response that can be reasonably fit by an exponential, and then growing the region until the fit quality starts to degrade significantly.

Figure 13 shows the parameter fits to the principal axis polarizabilities for the half shell used in our previous examples. The symbols in each plot are the observed $\beta_i(t)$, with color coding the same as in Figure 10. The lines are the parametric fits to the data. The fit to the early time response starts out solid, then changes to dashed as the actual polarizability starts to diverge from algebraic behavior. The exponential fit to the late time response ends up solid, but is shown dashed in the region where the polarizability is better represented by the algebraic form. Interestingly, the transition from algebraic to exponential is fairly rapid, so the two solid curves appear continuous in these plots. The fit parameters are shown in the table at the lower right of the figure (times are in msec), along with a picture of the target. The time domain parameterization for a bent over half shell is shown in Figure 14. The $\beta_3$ response is somewhat

different in this case than in the previous example, presumably because the $\beta_3$ face is no longer flat. Also note that in this example there is a slight gap in the early-late transition for $\beta_2$. The target for Figure 15 is one of the horse shoes recovered at Camp Sibert. Note that the early time fit does not converge for $\beta_3$. This is because in this case the magnetic crossover happens too quickly to be resolved by the MM-0601 TEM array. By the time we are measuring the response at 0.04 msec, it is well into the $t^{-3/2}$ regime. The GEM-3 is somewhat complementary to the MM 0601 TEM array here. It measures out to ~50 kHz, and so should be able to resolve magnetic crossovers an order of magnitude earlier, corresponding to $\tau_M$ values down to about $(2\pi\times 50\text{ kHz})^{-1} = 0.003$ msec.

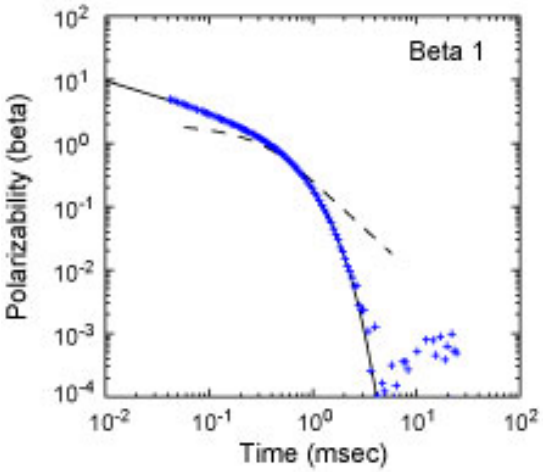


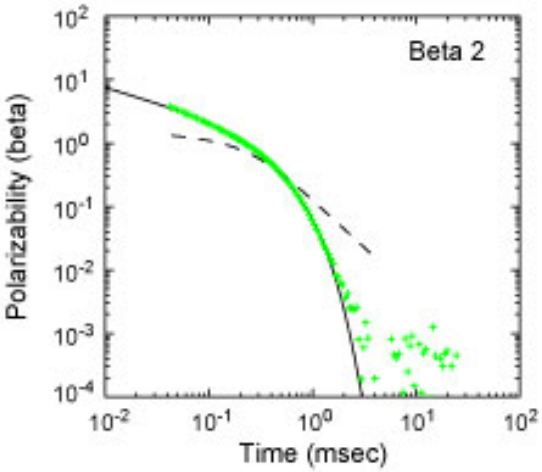


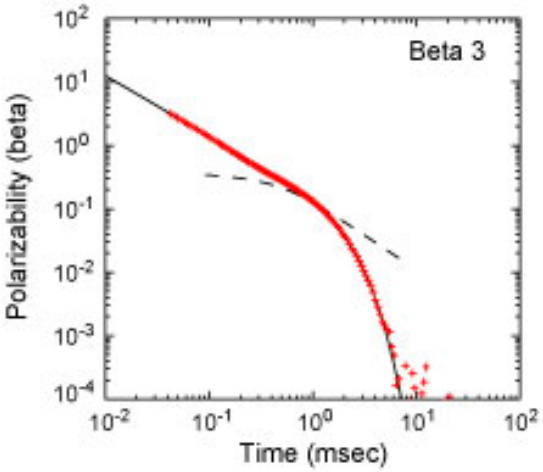


| $\beta$ | 1 | 2 | 3 |
|---|---|---|---|
| $a_M$ | 1.88 | 1.84 | 987 |
| $\tau_M$ | 0.26 | 0.17 | 0.14 |
| $\gamma$ | 2.4 | 2.1 | 0.1 |
| $a_0$ | 2.03 | 1.51 | 0.38 |
| $\tau_0$ | 0.42 | 0.31 | 0.87 |

**Figure 13. Parameter fits to principal axis polarizabilities for the clutter item used in the examples in Figure 4 and Figure 10.**

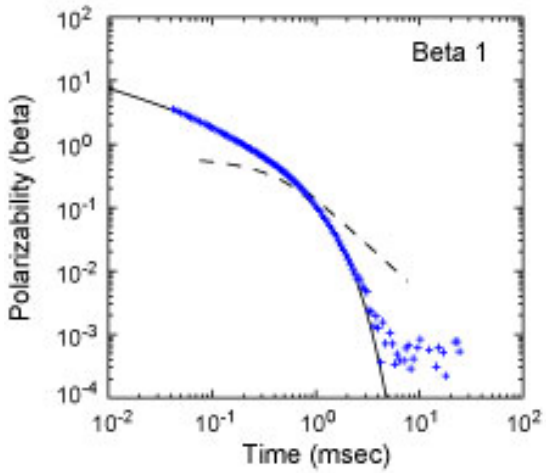


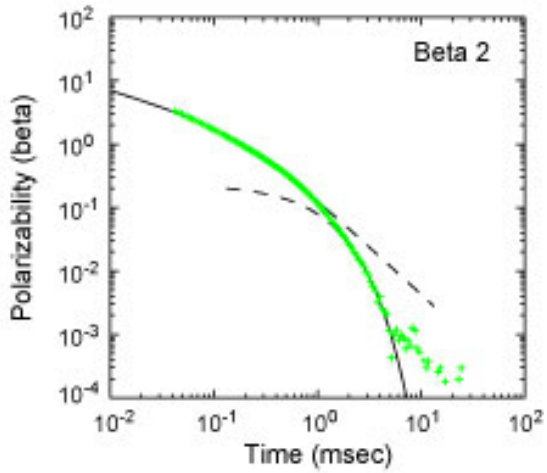


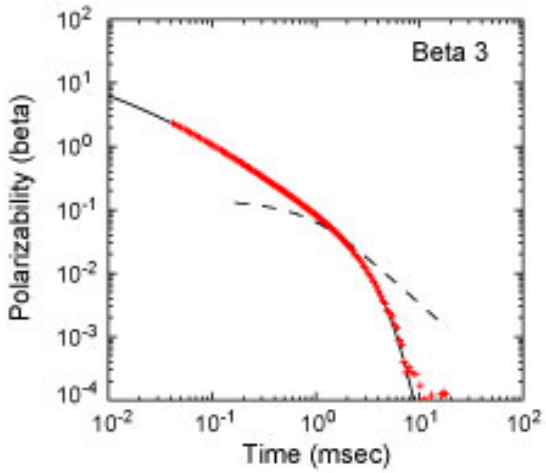


| $\beta$ | 1 | 2 | 3 |
|---|---|---|---|
| $a_M$ | 1.77 | 1.63 | 2.11 |
| $\tau_M$ | 0.19 | 0.19 | 0.14 |
| $\gamma$ | 1.3 | 1.3 | 0.7 |
| $a_0$ | 0.63 | 0.23 | 0.15 |
| $\tau_0$ | 0.55 | 0.93 | 1.21 |

**Figure 14. Parameterization of time domain response for a bent over half shell.**

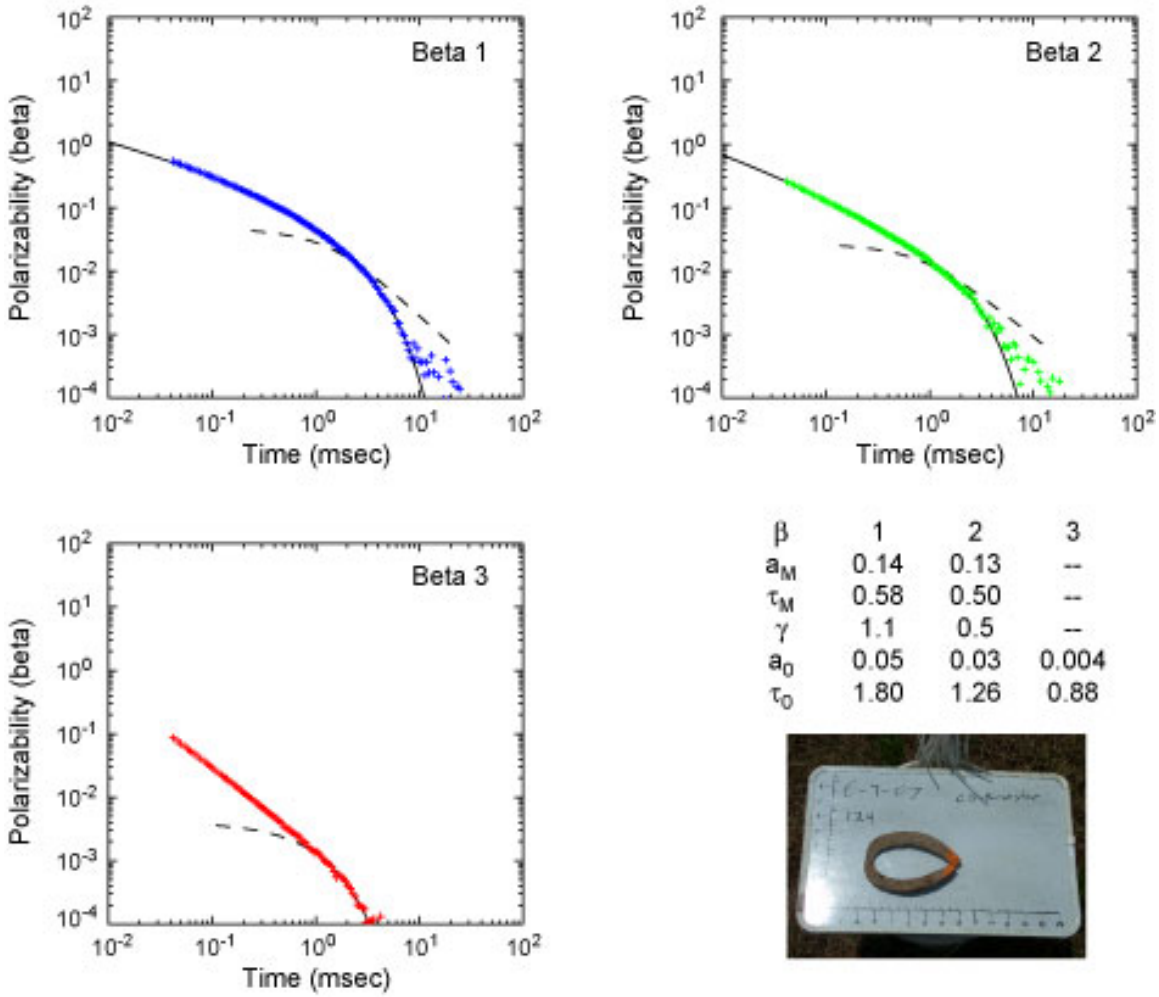


| $\beta$ | 1 | 2 | 3 |
|---|---|---|---|
| $a_M$ | 0.14 | 0.13 | -- |
| $\tau_M$ | 0.58 | 0.50 | -- |
| $\gamma$ | 1.1 | 0.5 | -- |
| $a_0$ | 0.05 | 0.03 | 0.004 |
| $\tau_0$ | 1.80 | 1.26 | 0.88 |

**Figure 15. Parameterization of time domain response for one of the horse shoes recovered at Camp Sibert.**

## 4. Parameter Regimes for Clutter Items

Feature-based classification is based on the premise that the parameters characterizing the EMI signatures of different types of objects will occupy different regions of the parameter space. This chapter sets about identifying regions of parameter space which correspond to different classes of munitions or clutter items. There are obvious size differences among the distinct clutter classes. These are captured by the net polarizability (§4.1). In addition to the size differences, there can also be substantial differences in the shapes of the respective decay curves, which is addressed in §4.2.

### 4.1. Net Polarizability

All things being otherwise equal, the polarizability of an object should scale in proportion to the volume displaced by the object [10]. We define the net early time polarizability as the sum of the three principal axis polarizabilities ($\beta_1$, $\beta_2$, $\beta_3$),

$$P = \Sigma\beta_i(t), \tag{22}$$

averaged over decay times from 0.04 msec to 0.06 msec. Histograms of the distribution of net polarizability for the entire set of clutter items listed in Table 1 are shown in Figure 16. The black line shows the distribution for the entire set of clutter items; different subgroups (mortar fragments, cultural clutter, range scrap and projectile fragments) are indicated by the colored lines. The overall distribution is heavily skewed by the mortar fragments recovered from Camp Sibert. The peak at about ten is due to half shells, the peak at about three corresponds to base plates, and that just below one has a significant contribution from mortar nose fragments along with cultural clutter. The cultural clutter items are broken down by site in Figure 17. The histogram for cultural clutter from the Lake Success Business Park (LSBP) redevelopment project is shown in blue, and that for the cultural clutter from Camp Sibert is shown in red. The LSBP site has a mix of agricultural, industrial and civil items. The Camp Sibert cultural clutter is mostly agricultural, and appears to have a somewhat tighter net polarizability distribution than LSBP.

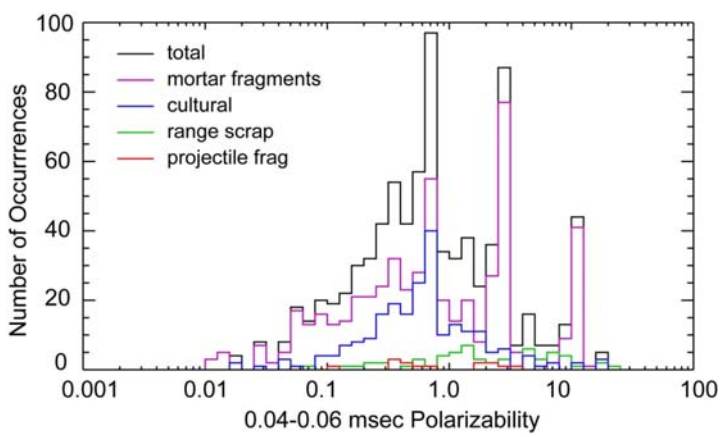


**Figure 16. Distribution of net polarizability for clutter items listed in Table 1.**

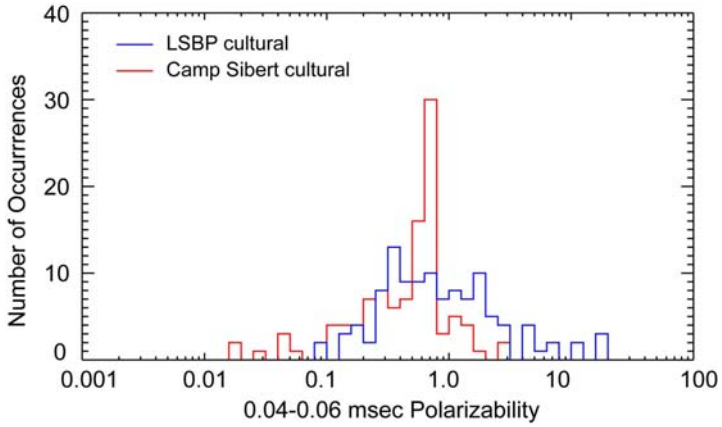


**Figure 17. Breakdown of cultural clutter by site.**

## 4.2. Decay Curve Parameters

In addition to the obvious size differences among the distinct clutter classes, there are also substantial differences in the shape of their characteristic decay curves. Figure 18 shows principal axis decay curves for (a) half shells, (b) base plates, (c) nose frag and (d) some of the small, thin-walled fragments from the front part of the mortar seen in Figure 1(c). The half shells' TEM response includes both algebraic and exponential regimes in our 0.04-25 msec measurement range. The baseplates and nose frag, though smaller than the half shells, are substantially thicker chunks of metal, and their measured response lies entirely in the algebraic regime. The measured response of the small fragments is mostly exponential. Each of these clutter types lies in a distinctly different region of the parameter space that describes the general TEM response.

The two-component response model introduced in §3.2 parameterizes the decay curve in terms of surface and body mode amplitudes and time scales. Figure 19 shows the distribution of surface mode and body mode amplitudes for various clutter objects determined from two-component model fits to their principal axis polarizabilities. Each item is represented by three points on the plot, corresponding to fits to its three principal axis polarizabilities. The three points are connected by colored lines for selected examples of different clutter types. If, instead of inverting the TEM array data and fitting the resultant polarizabilities with the two-component model, we had fit individual measurements from monostatic Tx/Rx array elements, then the data points would scatter around the areas marked out by the lines. The specific target examples corresponding to the lines are shown in Figure 20 along with their appropriate color code. A 76 mm projectile (which has only two unique polarizabilities) is shown by the black line in Figure 19. The complete half shells (magenta), occupy a well defined region of modal amplitude space. The cluster of points with surface mode amplitudes around $10^3$ and body mode amplitudes between 0.1 and 1 corresponds to excitation perpendicular to the more-or-less flat surface of the half shell. For edge-on excitation, the surface mode amplitude is several orders of magnitude smaller, while the body mode amplitude is a bit larger. The nose frag (cyan) and base plates (red) also occupy clearly distinguished regions of modal amplitude space. Miscellaneous broken fragments (blue, orange) and cultural items such as the broken baler tine (green) have modal amplitudes spread over more general regions.

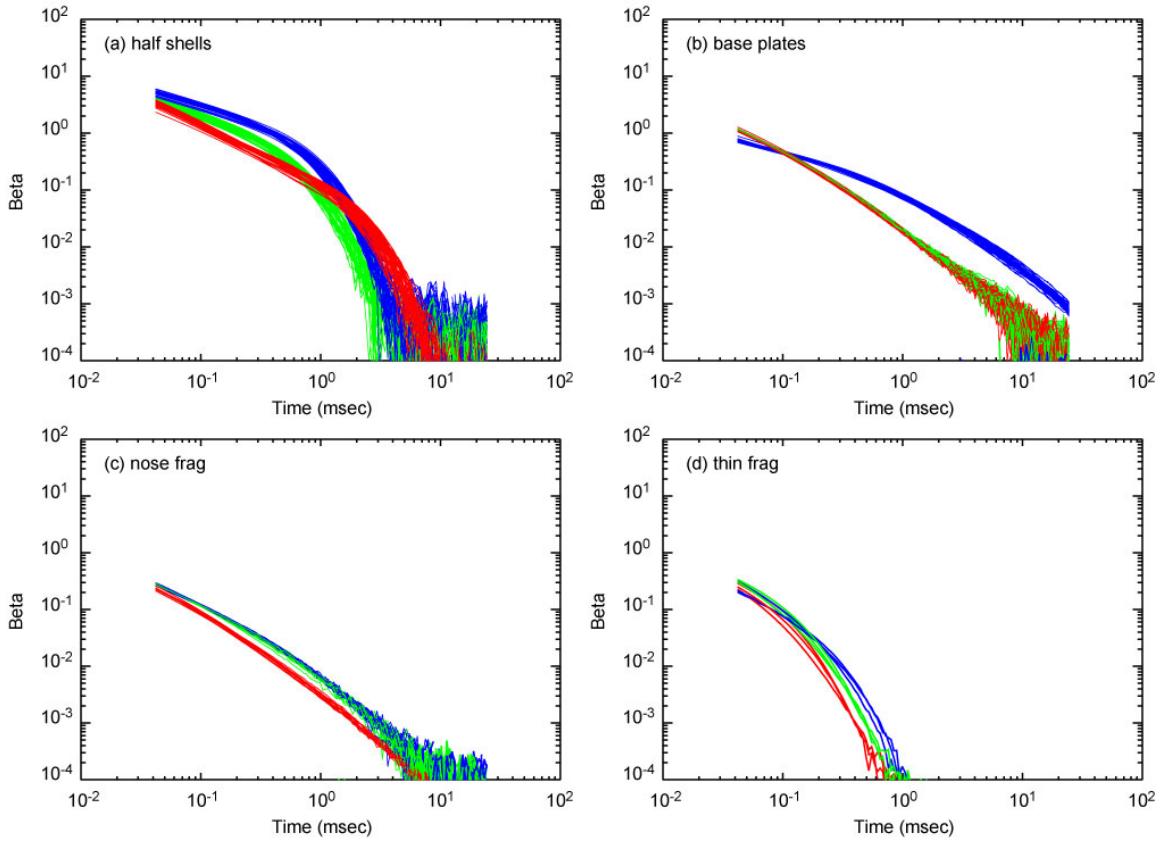


**Figure 18. Principal axis decay curves for different classes of clutter.**

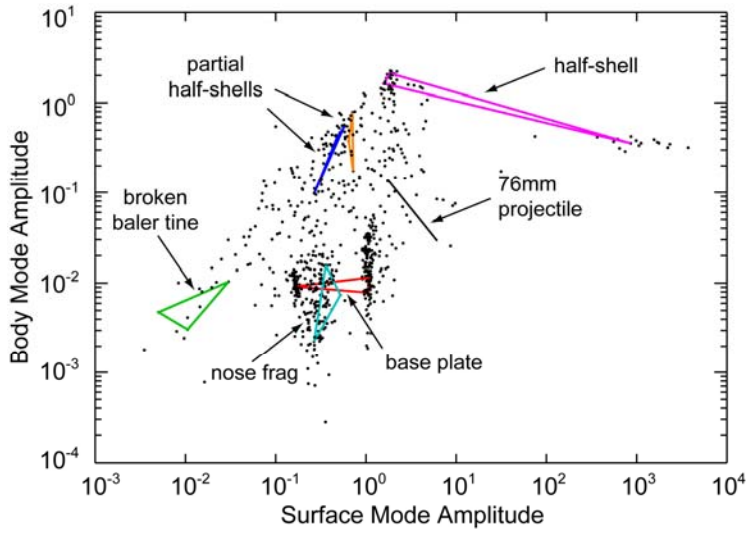


**Figure 19. Distribution of modal amplitudes for various clutter items compared with modal amplitudes for a 76 mm projectile.**

**Figure 20. Color-coded examples of different clutter types.**

Distributions of surface and body mode time scales for the clutter items are shown in Figure 21. The histograms on the left show distributions of surface mode and body mode time scales taken separately. They are plotted only over the range from 0.04 msec to 25 msec, corresponding to the EMI decay range measured by the MTADS TEM array. As it turns out, the array only resolves the surface mode time scale for about ½ of the clutter polarizabilities. The other half have at least one surface mode time scale that is too small to be determined by fitting the TEM data with the two-component model, so the data tend to be censored as the surface mode time scale approaches 0.04 msec. The body mode time scale is resolved for almost all of the data. The scatter plot on the right shows the joint distribution of the time scales. As in Figure 19, selected targets have their principal axis modal time scales connected by colored lines, using the same color scheme. In this

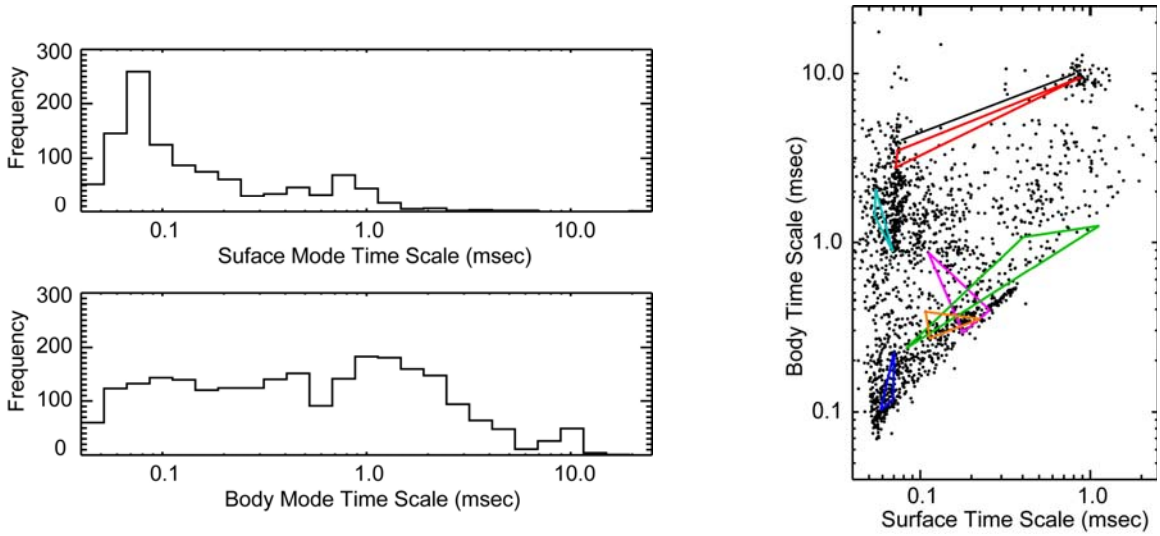


**Figure 21. Surface and body mode time scale distributions for the various clutter items.**

slice of parameter space, the base plates (*e.g.* as shown by the narrow red triangle towards the top of the plot) look very similar to the 76 mm projectile represented by the black line right above the red triangle.

The surface mode time scale is determined by the shape and composition of the target and its orientation relative to the EMI primary field. Figure 22(a), reproduced from [23], shows surface mode time scales for 4:1 aspect ratio steel cylinders. The cylinder diameters (d) range from 0.6 cm to 15 cm. Results are shown for axial and transverse alignment relative to the primary field. The time scale increases in proportion to the diameter squared, and the time scale for axial excitation is roughly 30 times larger than the time scale for transverse excitation. The surface mode time scales for typical munitions items behave similarly. Figure 22(b) shows the body mode time scale as a function of material thickness (h) for a variety of clutter items. Data are shown for the three principal axis responses for each item. For each item, the median value is shown by the symbol and the line connects the minimum and maximum values. On average, for h < 1 cm the body mode decay time scales as the second power of material thickness, with considerable scatter among the principal axes. Two thirds of the variance in the median decay time about the regression line can be accounted for by variations in the overall size of the object. Controlled for thickness, more material generally results in longer decay times.

Some specific clutter classes or types occupy restricted areas of response time parameter space, while more general classes spread out over the entire space. This is illustrated by Figure 23. Distributions of the surface and body mode times scales for mortar fragments are shown on the left. The response times for base plates, nose frag and body fragments (half shells and pieces of half shells) tend to cluster in distinct areas of the parameter space. (Recall that we are plotting principal axis response times, hence the base plates occupy two disjoint areas corresponding to axial and transverse excitation, *etc.*) Response times for the cultural items and range scrap, on the other hand, tend to spread out over larger regions of the parameter space.

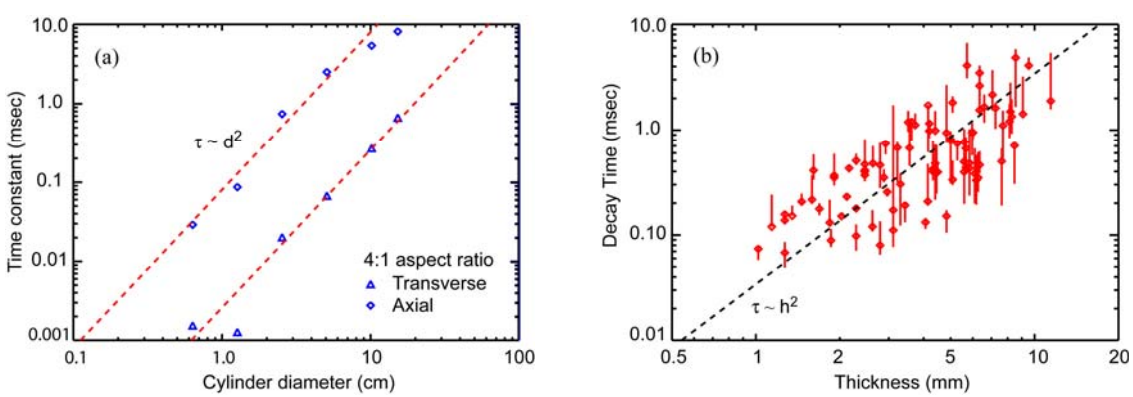


**Figure 22. (a) Surface mode time scales for 4:1 aspect ratio cylinders. (b) Body mode time scales *vs.* material thickness.**

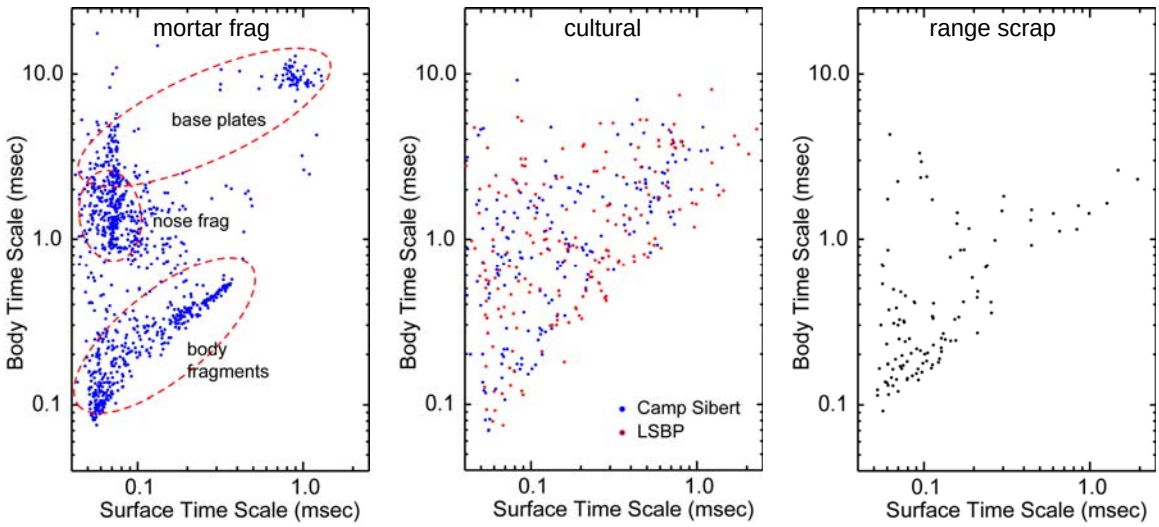


**Figure 23. Surface and body mode time scales for different clutter types.**

## 5. Position-Independent Processing of EMI data

Traditional approaches to classification rely on calculating principal axis polarizabilities by inverting spatially mapped EMI data collected over the target. The inversion process is very sensitive to errors in the data and is especially sensitive to errors in the relative locations of the sensor readings. We have explored the use of position-independent processing approaches to classification in this project. The approach is based on EMI signal attributes determined from simple parametric representations for the EMI signals measured above typical UXO or clutter items and how these parameters vary as the sensor is moved about over the item. Position-independent processing is amplitude-independent processing. We use only the shapes of the responses observed at various locations above the object, and do not particularly care where the measurements were taken. The only requirements are that the signals are relatively strong (roughly six times the measurement noise level appears adequate), and that we get a representative sample of the possible response shapes.

The plots shown in §4.2 give some idea of how this might work. Ratios of the body and surface mode amplitudes will vary with the target shape and the sensor/target geometry, but are independent of the sensor/target range, and hence are potentially useful for robust (position independent) processing and classification. The surface and body mode time scales are determined by factors relating to the shape and composition of the target, and its orientation relative to the sensor but not by its distance from the sensor. The data points in those plots are from fits of the two-component model to principal axis polarizabilities. However, for arbitrary sensor/target orientations, time scales from two-component model fits to the raw response data should scatter around the regions bounded by the corresponding principal axis values. A set of measurements over some target would then produce a trajectory of points in the parameter space of surface and body mode time scales. Figure 24 shows principal axis time scales for 40 mm and 76 mm projectiles and a 40 mm grenade (red lines) and for a variety of cultural clutter items (blue dots). The principal axis time scales are connected by lines as before for some of the clutter items. The time scale trajectories for the munitions items would be expected to follow upward sloping lines like the red lines connecting the principal axis values. Cultural items (and also range scrap) would exhibit a wide variety of trajectories, many which would likely be quite distinct from those corresponding to munitions items.

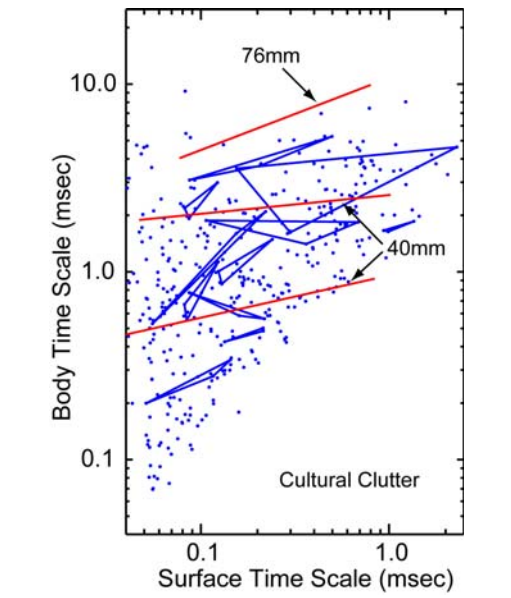


**Figure 24. Surface and body mode time scales for cultural clutter compared with munitions items**

While the two-component model provides a representation of EMI data which explicitly comprehends the basic physics of the response, it uses a lot of parameters, and it can fail to give reliable estimates for parameter values that lie outside the measurement range of the sensor. Consequently, we have explored the use of the empirical parameterizations referred to earlier.

## 5.1. Empirical Parameterization

The three-parameter model

$$S(t) = a\, t^{-\gamma}\, e^{-t/\tau} \tag{23}$$

introduced by Pasion and Oldenburg [13] combines the algebraic and exponential characteristics of the EMI response and can be used to represent the response for all but the earliest part of the eddy current decay. Figure 25(a) shows the measured response for the 4.2 inch mortar aligned transverse to the primary field along with the Pasion-Oldenburg model fit to the data. The model fit is shown as a solid curve during the measurement time range 0.04 msec to 25 msec and dashed for times outside that range. The curve deviates slightly from the measured response at early times. This is shown more clearly in Figure 25(b), which compares the Pasion-Oldenburg model fit to the 4.2 inch mortar EMI response with the complete surface and body mode representation. The basic problem is that as $t \rightarrow 0$ the EMI response must behave as $t^{-1/2}$ [20, 21] whereas the power law in the Pasion-Oldenburg fit to the 4.2 inch mortar response is fixed at $\gamma = 1.06$. In its original form, the model included an additional constant in the algebraic term which could bend the response down and give a better fit at early times. As a practical matter, though, equation (23) gives a reasonably accurate representation of the response over our measurement interval (0.04 - 25 msec) and is suitable for our purposes.

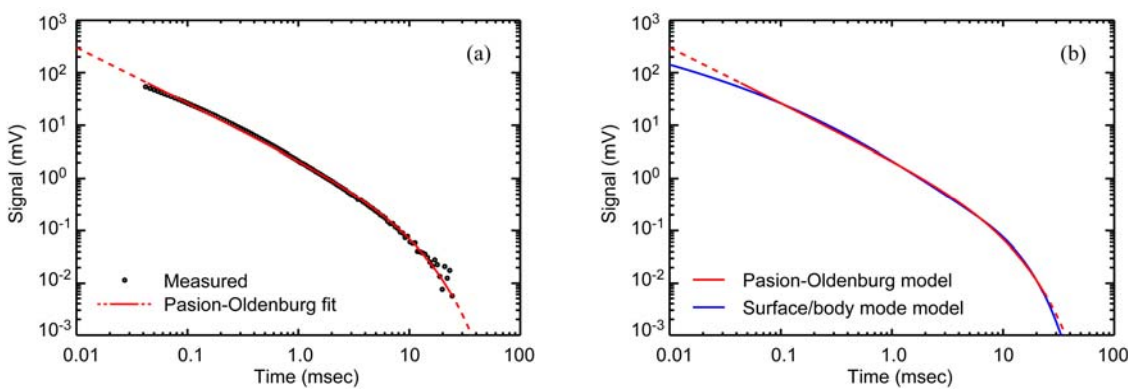


**Figure 25. (a) Pasion-Oldenburg model fit to the EMI response of a 4.2 inch mortar aligned transverse to the primary field. (b) Comparison between the two-component and Pasion-Oldenburg model fits to the 4.2 inch mortar response.**

The fixed power law is a compromise that captures the average behavior in the magnetic surface mode regime. For any object, the exponent $\gamma$ will be related to the surface mode time scale $\tau_M$ in a way that depends on the object's physical properties and the averaging time interval, which extends from the start of the measured response to the time at which body modes take over the response. This is illustrated in Figure 26, which shows the relationship between the Pasion-Oldenburg exponent $\gamma$ and the magnetic crossover time $\tau_M$ for measurements above a 4.2 inch mortar and a 60 mm mortar.

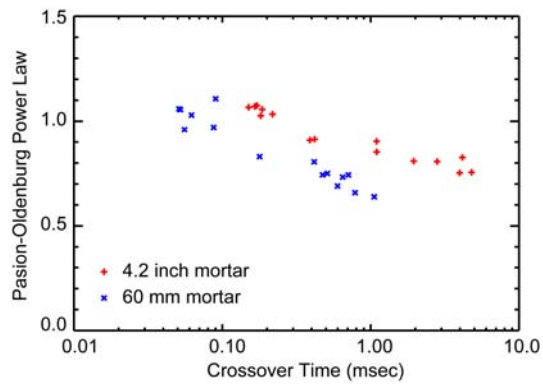


**Figure 26. Pasion-Oldenburg exponent γ compared to the magnetic crossover time $\tau_M$ for model fits to EMI data collected above a 4.2 inch mortar and a 60 mm mortar.**

## 5.2. Parameter Values

Distributions of the Pasion-Oldenburg power law (γ) and decay time (τ) parameters for various munitions and clutter items are shown in Figure 27 and Figure 28. For the munitions items, each plot shows γ *vs.* τ values for Pasion-Oldenburg model fits to MTADS TEM array data collected with the target at different orientations and depths below the array. We only used the central nine elements (3x3) of the 25 element (5x5) TEM array. The number of times each munitions item was measured with the array is shown in parentheses. Individual data points correspond to monostatic measurements from the central core 3x3 subarray. However, we only plot data for those Tx/Rx pairs which have signal strength at 216 μsec greater than 1 mV (chosen for consistency with the analysis centered on the EM61 time gates in §6). For example, the 105 mm projectile (lower right plot) was measured six times, each time at a different orientation and/or distance below the array. There are a total of 54 data points in the plot – for each measurement, all nine core Tx/Rx pairs had signal levels greater than 1 mV at 216 μsec. The 37 mm projectile (upper left plot) does not produce a strong response over the entire core area. It has a smaller footprint because it must be closer to the array to produce a good, strong signal. It was measured 14 times, but there are only 33 data points – on average only two or three array elements had a response greater than 1 mV at 216 μsec for any given orientation/depth combination.

For the munitions shown in Figure 27, higher power laws generally correspond to measurements where the primary field is directed more or less transversely to the object, while lower power laws correspond to more axial excitation (compare the axial and transverse polarizabilities in Figure 11(b)). Decay times scale with the size of the munitions, reflecting a general trend for the larger items to have thicker walls and correspondingly slower eddy current decay rates.

The clutter items in Figure 28 are grouped by class. One TEM array measurement using the core 3x3 subarray was taken over each item. The same constraint on signal amplitude was used for the clutter items. The number of different items in the class for which data were collected is noted on each plot. Depending on the size of each item, it may contribute anywhere from one to nine data points to the plot. Range scrap (relatively thin-walled blown-up scraps of steel) exhibits a distinctly different γ *vs.* τ distribution than the munitions, as do the half shells. The horseshoes

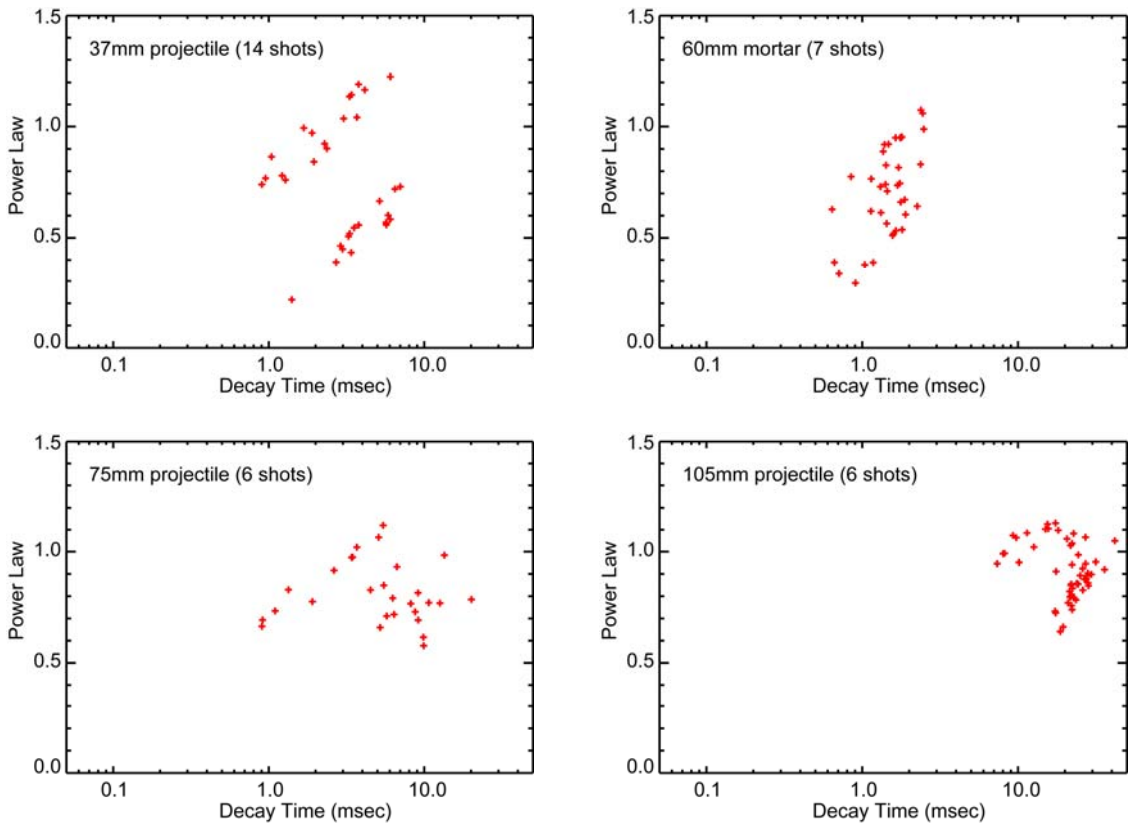


**Figure 27. Pasion-Oldenburg power law (γ) and decay time (τ) parameters for various munitions items.**

and broken pieces of horseshoes appear parametrically similar to the 75 mm projectiles, and the γ *vs.* τ distribution for the base plates has some similarity to the distributions for the munitions items. Generally speaking, however, there appear to be enough differences between the parameter distributions for munitions and clutter items to support some level of classification and discrimination.

## 5.3. Parameter Trajectories

The EMI response at any point over a munitions item can expressed in terms of a pair of polarizability functions corresponding to axial and transverse excitation. Using the Pasion-Oldenburg model, these functions can be reduced to points in the (τ, γ) parameter space. Position-independent processing focuses on combinations of decay time and power law parameter values τ and γ that describe the shapes of the axial and transverse polarizability functions. Signals measured at intermediate excitation and/or observation angles can be expressed as linear combinations of the axial and transverse polarizabilities. In general they can also be approximated quite well using the Pasion-Oldenburg model. Thus the shape parameters τ and γ for any sensor/object alignment should lie at some point on a specific curve or trajectory in this parameter space that passes through the points determined by the axial and transverse polarizabilities. Strictly speaking, linear combinations of the Pasion-Oldenburg functions represented by equation

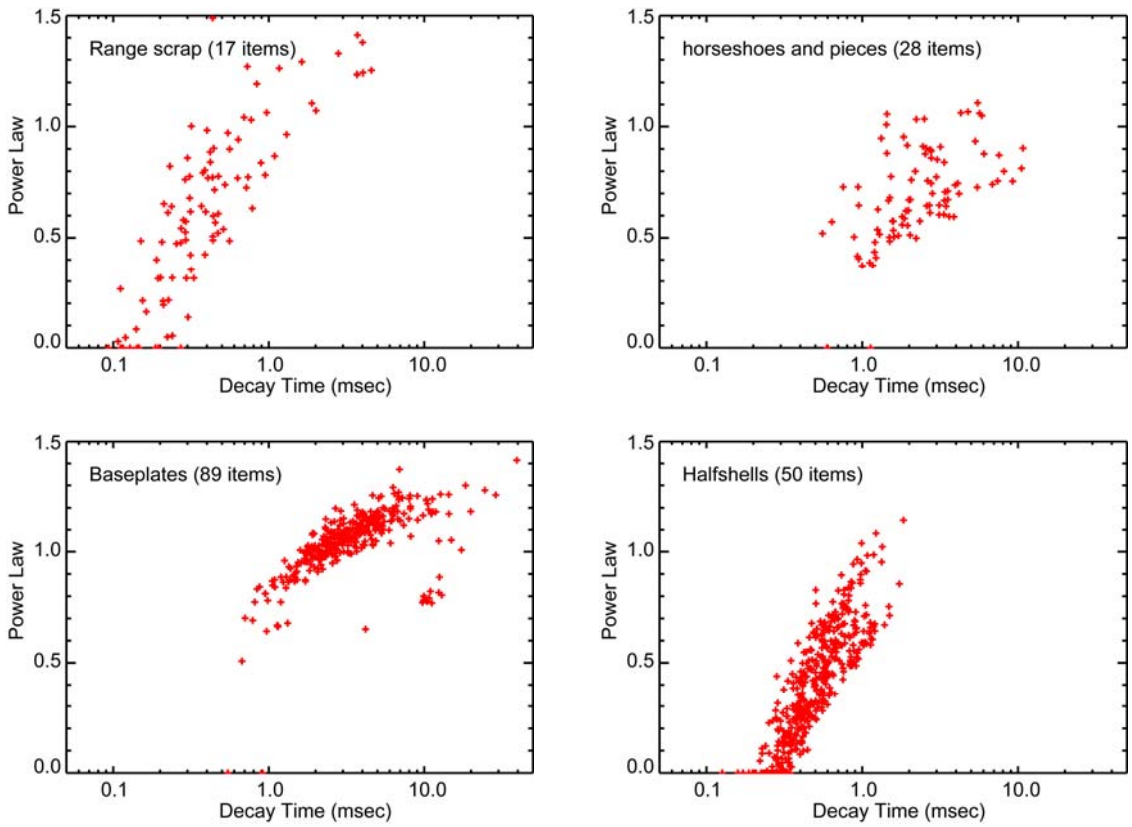


**Figure 28. Pasion-Oldenburg power law (γ) and decay time (τ) parameters for several types of clutter items.**

(23) are not themselves Pasion-Oldenburg functions. However, the model is sufficiently accommodating that the approximation works.

This is illustrated in Figure 29(a). The crosses (+) in this plot show the distribution of power law and decay time parameters for the set of response curves shown in Figure 11(a). The circles (o) show the corresponding parameters determined by fitting the principal axis polarizabilities shown in Figure 11(b). They are color-coded as in Figure 11(b). The trajectory traced out by τ-γ fits to different linear combinations of the polarizabilities is shown by the curve. (We used the average of the two transverse polarizabilities in calculating the trajectory.) The individual points are seen to follow the calculated trajectory. Note that the trajectories are curved. They do not follow a straight path between the extremes defined by the principal axis polarizabilities.

The power law (γ) and decay time (τ) parameters can be calculated directly from unmapped EMI data and represent target attributes that can used for classification. EMI responses for different UXO items will lie on different trajectories in the (τ, γ) parameter space, trajectories which reflect the UXO item's physical attributes (size, length to diameter aspect ratio, wall thickness, *etc.*). Figure 29(b) shows the parameter trajectories for the 4.2 inch mortar and for a 60 mm mortar. They are similar, but displaced in the τ dimension. As seen in Figure 28, the EMI responses for clutter items will inhabit their own regions of (τ, γ) space determined by their physical attributes.

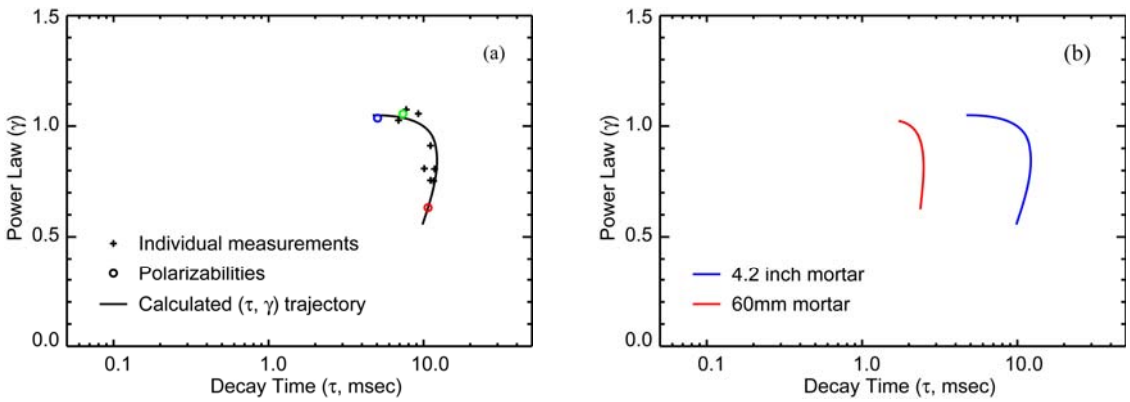


**Figure 29. (a) Decay time (τ) and power law (γ) parameters for the 4.2 inch mortar. The trajectory is calculated by fitting the Pasion- Oldenburg model to linear combinations of the principal axis polarizabilities. (b) Parameter trajectory corresponding to linear combinations of the principal axis polarizabilities for the 4.2 inch mortar compared with that for a 60 mm mortar.**

In general, the responses for irregularly shaped objects will not follow a simple trajectory, but rather will spread over some region. For example, the cluster of parameter values for the mortar fragments (half shells) in Figure 30 is well separated from the area of parameter space populated by the 4.2 inch mortar data.

## 5.4. Polarizability Calculations

In conventional processing schemes the principal axis polarizabilities are calculated by inverting spatially mapped EMI data collected over an object. Position-independent estimates of the shapes of the axial and transverse polarizability functions can be calculated from unmapped EMI response data by inverting the procedure for calculating the (τ, γ) trajectory from the parameter values for the axial and transverse polarizabilities. The position-independent inversion proceeds by systematically varying (τ, γ) pairs for the axial and transverse polarizabilities until the trajectory for linear combinations of the polarizabilities best matches the (τ, γ) values for the set of responses measured over the object. Figure 30 shows examples of polarizability shapes calculated this way for the 4.2 inch mortar (left) and the 60 mm mortar (right). The polarizabilities are normalized to a maximum value of one since the position-independent processing does not calculate the amplitude parameters. There is a near perfect match between conventionally calculated polarizabilities and position-independent estimates for the 60 mm mortar. The slight mismatch for the 4.2 inch mortar arises because the data did not include direct axial illumination of the mortar. This is an important aspect of the notion of amplitude-independent or position-independent processing. Dipole inversion can recover the principal axis polarizabilities even if the data do not include instances of both pure axial and transverse excitations. If the data do not include both, or include geometries that come close to including both, then position-independent processing generally cannot reproduce the responses for axial and transverse excitation. It stops at the most extreme linear combination of the polarizabilities available in the data.

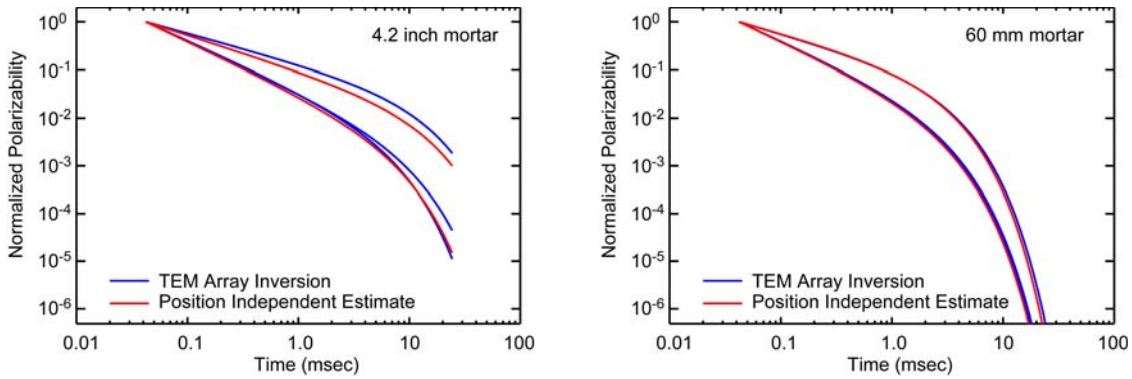


**Figure 30. Normalized polarizabilities for a 4.2 inch mortar (left) and a 60 mm mortar (right) calculated by conventional EMI inversion (blue) and by fitting parameter trajectories to unmapped EM data (red).**

## 6. Intermediate Time Response

In §5 we used the entire decay time interval measured by the MTADS TEM array, running from 40 μsec to 25 msec. Other sensors do not measure the EMI response over this entire interval. The Berkeley UXO Discriminator (BUD) measures eddy current decays from about 150 μsec to 1.5 msec [25]. The Geonics EM61 measures the response averaged over four time gates in roughly the same eddy current decay regime (216, 366, 660 and 1266 μsec). For the most part, these sensors do not measure the late stage exponential regime for most munitions items, and a Pasion-Oldenburg type of representation involving exponentials is not appropriate. However, we can still represent the EMI response in this regime with simple parametric models more appropriate to the algebraic decay generally observed during intermediate times.

### 6.1. Parametric Representation

Figure 31 shows an example of a simple parametric representation of the EMI response in the intermediate decay time regime. The symbols in Figure 31 show the EMI response for a transversely oriented 4.2 inch mortar (see Figure 25) re-sampled at the EM61 time gates. The curve shows a quadratic fit (in log/log coordinates) to the four plotted points using the equation

$$\log(S) = a_0 + a_1 \log(t/t_0) + a_2 \{\log(t/t_0)\}^2. \tag{24}$$

The fit is centered on $t_0 = 0.5$ msec so that the slope parameter $a_1$ roughly corresponds to the average power law over the measurement interval (0.216 to 1.266 msec), while the curvature parameter $a_2$ gives a measure of how much the slope varies over the interval. For munitions, we expect that $a_1$ will be around -1, shifting more towards -1/2 or -3/2 depending on whether the magnetic crossover time $\tau_M$ is larger or smaller than $t_0$. The curvature parameter $a_2$ will depend on both $\tau_M$ and the surface mode bandwidth. In this case, $a_1 = -1.16$ and $a_2 = -0.17$, while $\tau_M =$ 0.19 msec for the two-component model fit shown in Figure 25(a).

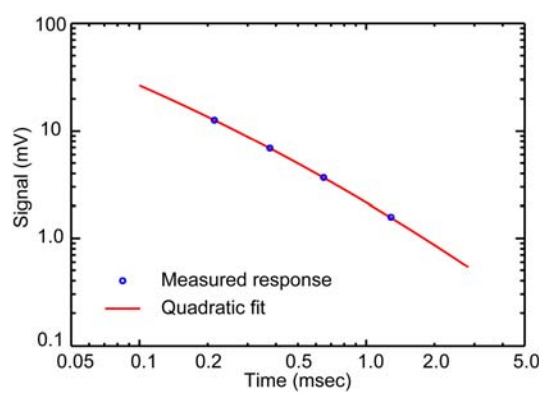


**Figure 31. Measured transverse 4.2 inch mortar response at EM61 time gates (symbols) and quadratic fit to the measured response (curve).**

## 6.2. Parameter Values

Distributions of the slope ($a_1$) and curvature ($a_2$) parameters for a thirty different munitions items (projectiles, mortars and rocket warheads) ranging in size from 20 mm to 155 mm are shown in Figure 32(a). The plot shows the results of a total of 1,254 fits of equation (24) to MTADS TEM array data collected with the various targets at different orientations and depths below the array. As in §5.2, the individual data points correspond to monostatic measurements from Tx/Rx pairs in the central region of the array having signal strengths at 216 μsec greater than 1 mV. Figure 32(b) shows the corresponding parameter values for aluminum munitions or submunitions and grenades, which tend to lie outside the cluster of points associated with the (primarily steel) projectiles, rockets and mortars.

The points in Figure 32(a) cluster rather tightly, unlike the spread for different munitions types with the Pasion-Oldenburg parameters evident in the plots in Figure 27. This is because the range of decay times used in the slope-curvature parameterization does not extend to late enough times to appreciate the different late stage decay rates appropriate to different munitions sizes. Corresponding plots for the various classes of clutter items from §5.2 are shown in Figure 33. The slope-curvature distributions for the half shells and the range scrap do not overlap much with the corresponding distributions for the munitions items in Figure 32(a), but the base plates and horseshoes cannot be distinguished from the munitions on the basis of their slope and curvature parameters.

We have compared the distributions of slope/curvature parameters for a subset of the clutter listed in Table 1 with the distribution for munitions items shown in Figure 32(a). We used a subset of 314 items including only 15% of the Sibert items so as to minimize their influence. A total of 1321 measurements had signal levels above the 1 mV threshold. Almost half (609) of these have slope and curvature parameters outside of the region occupied by measurements over the munitions items. Half of the clutter items (160 of 314) have responses that extend beyond the UXO area, and the parameter values of over 1/3 of the items (114 of 314) do not overlap the region associated with UXO at all. Pictures of 105 of the clutter items with parameter distributions disjoint from the UXO parameter distribution are included as Appendix A.

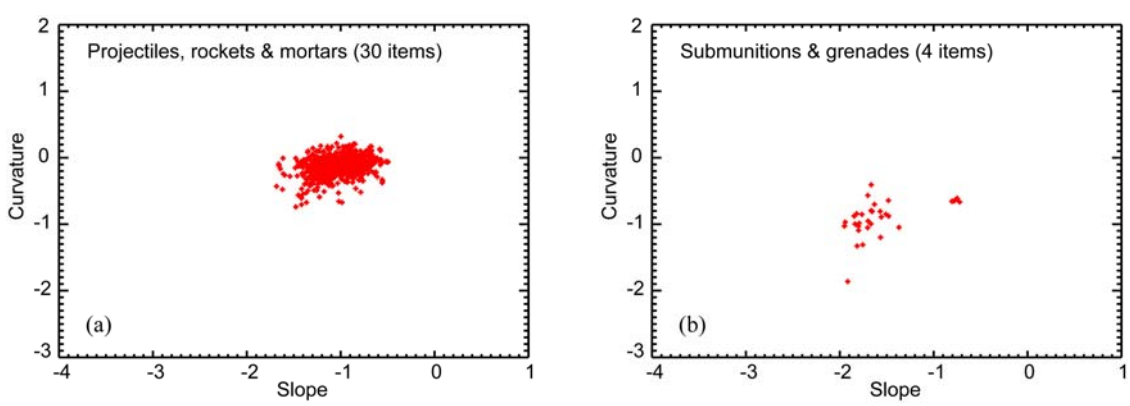


**Figure 32. Distribution of slope and curvature parameters for (a) projectiles, mortars and rockets and (b) submunitions and grenades.**

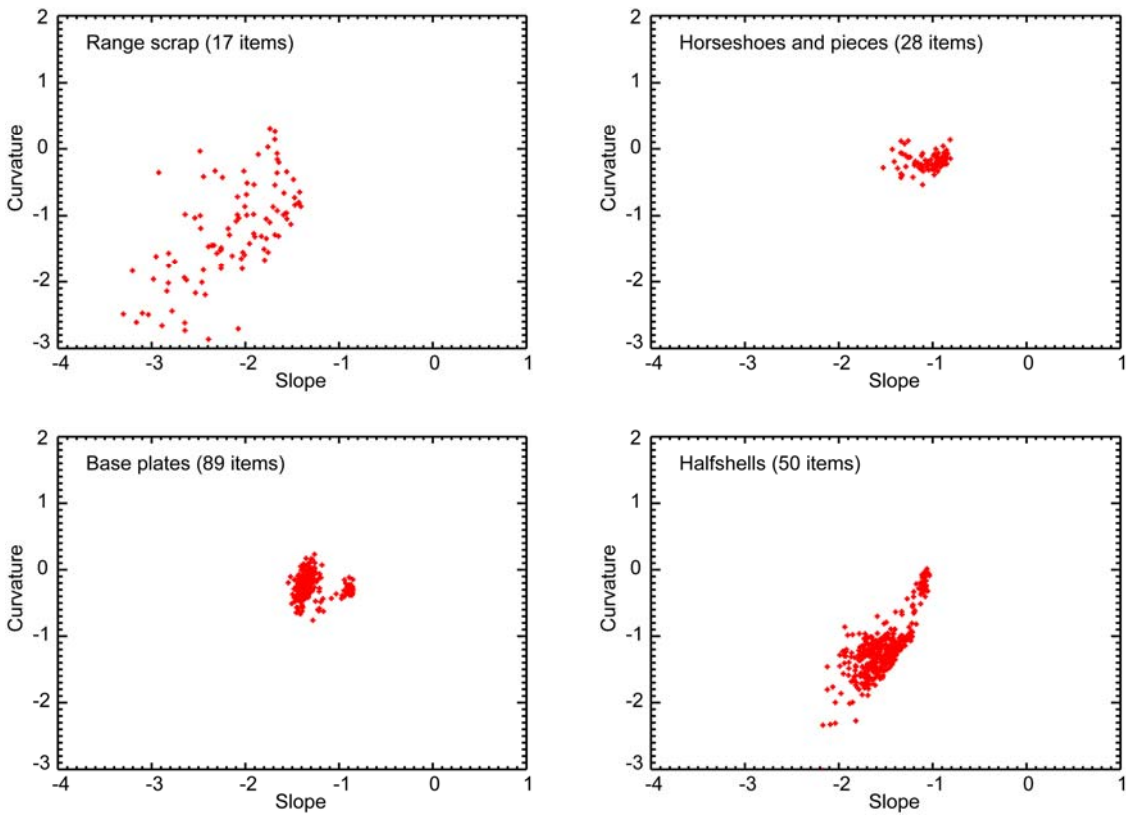


**Figure 33. Slope and curvature parameters for various classes of clutter items.**

## 6.3. EM61 Survey Data

As part of ESTCP Project MM-0413, we acquired the EM61 data collected by the Geophysics Group of Shaw Environmental and Engineering in 2003 at the Aberdeen Proving Ground (APG) UXO Test Site using the system shown in Figure 34. Ground truth for the open field at the test site was released in 2005, and the site has since been reconfigured. Shaw collected survey data using all four EM61 time gates. Other EM61 survey data sets that we acquired in that project were differential mode, which only covers the first three gates, and are therefore not really

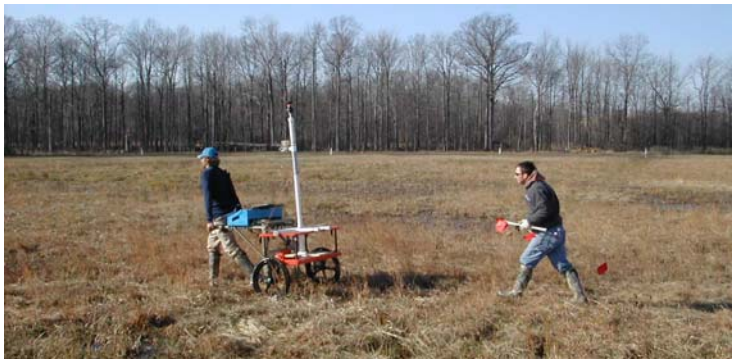

**Figure 34. Shaw EM61 system at Aberdeen Proving Ground Standardized Test Site.**

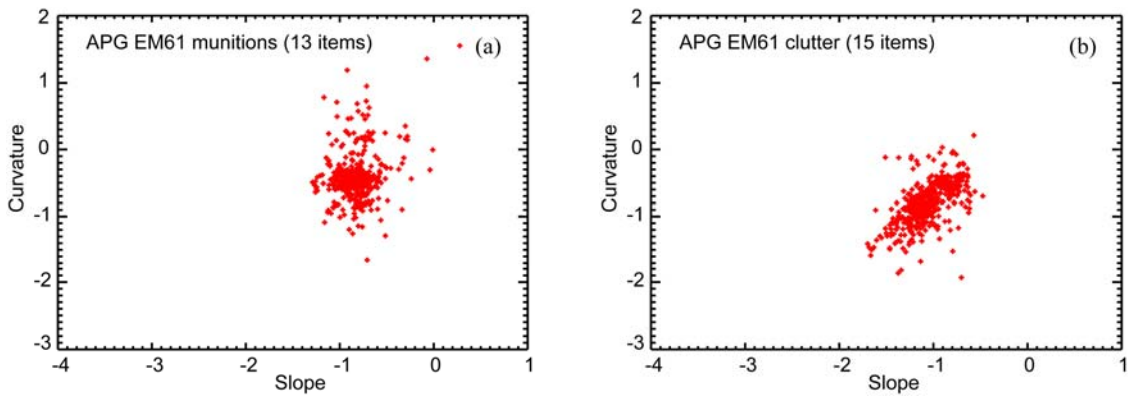


**Figure 35. Distributions of EM61 response slope and curvature for (a) APG munitions and (b) clutter items.**

suitable for our analysis. Distributions of the slope and curvature parameters extracted from the Shaw EM61 data over various munitions and clutter items in the APG Open Field are plotted in Figure 35. Pictures of the items are included in Appendix B. The parameter spread for the munitions items is considerably broader than for the TEM data in Figure 32(a). Presumably this reflects the basic problems with noise and leveling in survey data. Even so, the parameter values for the clutter items do extend beyond the general area occupied by the munitions parameters.

Although the EM61 parameter distributions from the survey data are more diffuse than were obtained using the MTADS TEM array data, they do seem to offer some limited UXO/clutter classification potential. Specifically, in cases where EM61 survey data is used to detect targets for later classification using cued systems, it may be possible to identify some high confidence clutter items directly from the EM61 survey data and thereby reduce the number of cued data collections that have to be done.

## 7. Bulk Magnetization

There are two basic components in the EMI response to munitions and clutter items: magnetization of the object by the primary field transmitted by the sensor and the evolution of eddy currents set up in the object by changes in the primary field. The results reported in §§4-6 dealt with the eddy current response, which does not exploit all of the information that is available in the EMI response. In this section we address that part of the EMI response that is associated with bulk magnetization of the target.

The magnetization response is only observed while the primary field is also present. It can be extracted from the in-phase part of our frequency domain response data (§2.2). To within a constant factor, the time domain and frequency domain responses are related by Fourier or Laplace transform pairs. The constant factor represents the bulk magnetization response, and it can be estimated by fitting a simple model to the measured frequency domain response [18, 23].

### 7.1. Demagnetizing Factors

An object's shape affects how it responds to magnetic fields. The effects are represented by demagnetizing factors that depend on the direction of the applied field relative to the object and are determined by the physical details of how the object responds to externally applied magnetic fields [8]. When an object becomes magnetized by an external field $H_0$, microscopic magnetic domains within the object distort and rotate towards alignment with the applied field. This results in a buildup of positive and negative magnetic poles on opposite sides of the object, creating a field $H_d$ opposed to $H_0$ within the object. The induced field $H_d$ is called the demagnetizing field because it always tends to oppose $H_0$. In the case of uniformly magnetized spheroids, the relationship between $H_d$ and $H_0$ can be expressed in terms of a demagnetizing or demagnetization tensor **N** [26]. The eigenvalues $N_i$ of the demagnetizing tensor are the demagnetizing factors for the principal axes of the spheroid, and $\Sigma N_i = 1$. For more general objects the demagnetizing field cannot be expressed in terms of a demagnetizing tensor. The magnetization responses in the principal axis directions can still be expressed in terms of demagnetizing factors, but the transformation rules for Cartesian tensors will not necessarily apply and the demagnetizing factors for the principal axes need not sum to one. For example, the sum of the demagnetizing factors for finite cylinders of moderate length to diameter aspect ratio is generally about 10% less than one [27].

Magnetized in a direction perpendicular to its surface, a thin piece of material will generally have a larger demagnetizing factor than a thick one because the surface magnetic poles are closer together. The plots in Figure 36 summarize pertinent information on the demagnetizing factors for disk- and rod-like objects. Figure 36(a) shows the dependence of the demagnetizing factor on length to diameter aspect ratio for cylinders and ellipsoids. The solid lines are interpolated from tabulated values for finite cylinders [27], while the dashed lines are calculated using the analytical formulae for ellipsoids [28]. Symbols are values determined from fits to the frequency domain response for 2.54 cm diameter steel cylinders. Figure 36(b) shows how the demagnetizing factor varies as a cylinder is rotated in an external field. The demagnetizing factor is smallest when the field is aligned parallel to the axis of the cylinder, and largest when the field is perpendicular to the axis. The demagnetizing factors shown by the data points in Figure 36 were calculated from frequency domain responses for axial and transverse excitation measured with a GEM-3 sensor. If $S(\omega)$ is the frequency domain response, then the demagnetizing factor N is given by

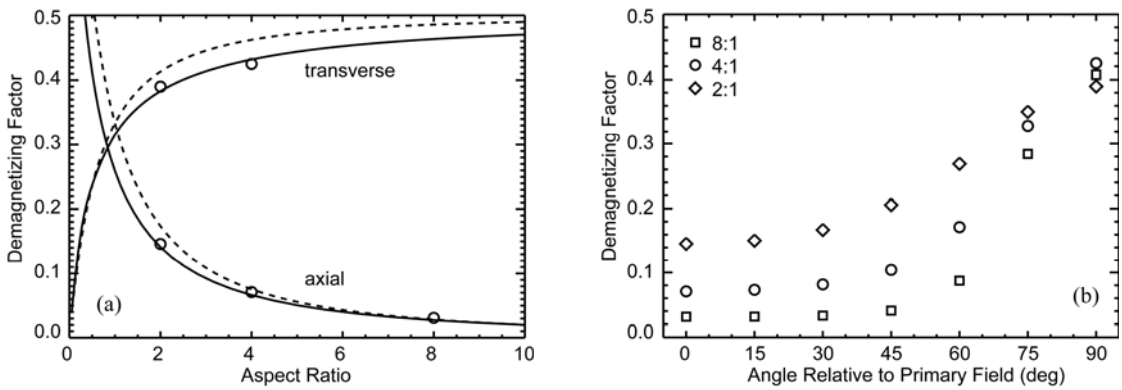


**Figure 36. (a) Demagnetizing factors for cylinders (solid lines) and ellipsoids (dashed lines) *vs.* length to diameter aspect ratio. Symbols are measured values for steel cylinders. (b) Effect of applied field direction on the demagnetizing factors for cylinders.**

$$N = \lim_{\omega \to \infty} \frac{S(\omega)}{S(\omega) - S(0)} . \tag{25}$$

The responses at $\omega = 0$ and $\omega \to \infty$ are estimated by first fitting the quadrature data to the imaginary part of the simple frequency domain response model [18].

$$S(\omega) = a_0 + a_1 \frac{(i\omega\tau)^\gamma - 2}{(i\omega\tau)^\gamma + 1} \tag{26}$$

then determining the constant offset by comparing the in-phase data with the corresponding real part of equation (26). The values of N for axial excitation are increased slightly for smaller, but still large relative permeability. The effect is less than 2.5% for a 4:1 aspect ratio cylinder with $\mu_R > 50$. The sum of the demagnetizing factors for the three principal axes $\Sigma N_i = N_{ax} + N_{tr} + N_{tr}$ equals 1 for the ellipsoids, but is generally less than 1 for cylinders. The deviation from one is greatest for small aspect ratios, with $\Sigma N_i$ increasing from 0.89 when the aspect ratio is one to about 0.97 for 10:1 cylinders. For the 4:1 cylinders in Figure 36, $\Sigma N_i = 0.93$.

## 7.2. Magnetization Responses of Munitions and Clutter

It has been observed that steel munitions items have demagnetizing factors comparable to those of comparable cylindrical objects [18, 23]. Figure 37 is a plot of demagnetizing factors calculated from in-phase frequency domain EMI measurements of various munitions and clutter items. The data in this figure are based on fits of equation (26) to the frequency domain principal axis polarizabilities of each object. The horizontal axis plots the average of the three demagnetizing factors for the object, and the vertical axis the largest one. There are 11 different munitions items

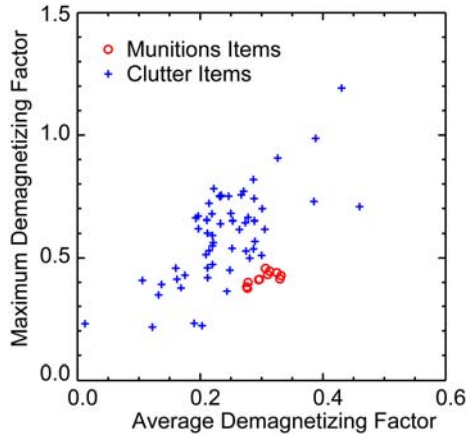


**Figure 37. Demagnetizing factors for munitions and clutter items.**

(20 mm, 40 mm, 57 mm, 5 inch, 152 mm and 155 mm projectiles, two 60 mm, an 81 mm and a 4.2 inch mortar, and a 2.75 inch rocket warhead) and 58 clutter items including a variety of exploded ordnance fragments, cultural items and range scrap. Values for the munitions items cluster close to the point (0.31, 0.43), which corresponds to the values for a steel cylinder with a four to one length to diameter aspect ratio. Values for the clutter items scatter over a much wider range, and the maximum demagnetizing factors for the clutter items are often significantly larger than for the munitions. These are consequences of the facts that the clutter items tend to be irregularly shaped and that many of them have one dimension significantly smaller than the other two.

## 8. Conclusions and Recommendations

This project is primarily about the shapes of the EMI response functions of munitions and clutter items, the differences between them, and the extent to which those differences are useful in classifying an unknown target as UXO or clutter. An extensive database of EMI signature data for munitions and clutter items has been assembled, and the data have been processed to extract parameters or features which characterize the EMI signatures of munitions and various types of clutter items (exploded ordnance fragments, range scrap and cultural clutter from agricultural, industrial and civil sources).

Processing of the EMI response data involves fitting the data to simple parametric models. We have developed a physics-based two-component model that has an algebraic form for the early time response paired with an exponential decay for the late time response. The two components (algebraic and exponential) in the model represent contributions to the response from magnetic surface modes and body modes. The shape of the response is controlled by the time scales of the two components: the magnetic crossover time ($\tau_M$) between the very early $t^{-1/2}$ regime and the intermediate time $t^{-3/2}$ regime of the magnetic surface modes, and the late stage exponential decay time ($t_0$) of the fundamental body mode. The surface mode time scale ($\tau_M$) is determined by the shape and composition of the target and its orientation relative to the EMI primary field. The body mode time scale ($t_0$) is determined primarily by the thickness of the material that the item is made of. Various types of munitions and clutter items can have quite distinctive distributions of $\tau_M$ and $\tau_0$ which are potentially significant for UXO/clutter classification. Importantly, $\tau_M$ and $\tau_0$ can be calculated directly for individual measurements of the EMI response at some point above an unknown target, enabling the use of classification schemes based on distributions of $\tau_M$ and $\tau_0$ or related parameters from sets of data collected over the target, without the need for spatial mapping of the data.

A simple empirical parameterization introduced years ago by Pasion and Oldenburg [13] can be used in a similar manner. This model combines the algebraic and exponential characteristics of the EMI response in a simple, straightforward way using a single power law exponent ($\gamma$) and an exponential decay time scale ($\tau$). The model is simpler than the complete two-component response model, which includes modal amplitude and bandwidth parameters. However, we have found that it can be used to adequately represent the response for all but the earliest part of the eddy current decay. As might be anticipated from the two-component model results, we find that distributions of the power law and exponential decay parameter values for various classes of clutter items are quite different from those of different munitions items. The trajectories of these parameter values that are swept out as a sensor is moved about over a munitions item are quite distinctive, and we have devised a simple procedure for estimating the shapes of the principal axis polarizability curves for munitions items from data collected as a sensor is blindly moved about over the item.

This last result suggests the interesting possibility of position-tolerant processing of EMI survey data. If the shapes of the principal axis polarizability curves are estimated directly from a collection of measured EMI responses over the target, then only the amplitudes remain to be determined to complete the description of the target's EMI response. Conventional dipole inversion of spatially mapped data determines principal axis polarizability shapes and amplitudes simultaneously, and is notoriously sensitive to mapping errors. It is possible that the inversion will be more robust to sensor location errors if only the amplitudes have to be calculated.

The basic conclusions still apply, albeit with some loss of potency, when the range of measured decay times is restricted. To investigate this, we downsampled the time domain data (collected using the MTADS TEM array) to the standard EM61 sensor's sampling gates centered at 216, 366, 660 and 1266 μsec. Since this decay range does not extend far enough to sample the exponential regime for many items of interest, we use a simple model that is quadratic in log(signal) *vs.* log(time) to fit the data. The two shape parameters (slope and curvature in log space) then correspond to the average power law over the measurement range and how much it changes over the range. The parameter distributions for munitions and clutter have some similarity to the distributions of the power law and exponential decay rate parameters, and it appears that some measure of position-independent classification should be possible even when the response is sampled over this restricted range.

A limited amount of EM61 survey data collected at the Aberdeen UXO Demonstration Site, along with supporting ground truth data, has been analyzed. The parameter distributions are somewhat more diffuse than those obtained using MTADS TEM array data, but still seem to offer some UXO/clutter classification potential. Specifically, in cases where EM61 survey data is used to detect targets for later classification using cued systems, it may be possible to identify some high confidence clutter items directly from the EM61 survey data and thereby reduce the number of cued data collections that have to be done.

The time domain data measures only the eddy current decay component of the EMI response of an object. However, there is another part of the response distinct from the eddy current response. Steel objects (like most munitions and clutter) become magnetized while the primary field is on. We have analyzed this bulk magnetization component of the response for munitions and clutter items using frequency domain data.

An object's shape affects how it responds to magnetic fields. The effects are represented by demagnetizing factors that depend on the direction of the applied field relative to the object and are determined by the physical details of how the object responds to externally applied magnetic fields. These demagnetizing factors are another amplitude-independent response parameter and can be determined by fitting the in-phase part of the frequency domain response with a simple model. Distributions of the demagnetizing factors for munitions and clutter items are distinctly different. This reflects very real shape differences. The munitions items are basically 4:1 aspect ratio cylinders as far as the magnetization response is concerned, and their demagnetizing factors cluster accordingly. Values for the clutter items scatter over a much wider range, and the maximum demagnetizing factors for the clutter items are often significantly larger than for the munitions. These are consequences of the facts that the clutter items tend to be irregularly shaped and that many of them have one dimension significantly smaller than the other two.

These findings have several implications for sensor design. Emerging EMI sensors such as the NRL TEM array and the Berkeley UXO Discriminator (BUD) do not measure the complete EMI response. Both are transient EM sensors and as such do not measure the bulk magnetization response. Nor do these sensors have adequate bandwidth to measure the complete eddy current decay response. We have found that for many UXO and clutter items the magnetic crossover time $\tau_M$ is not resolved by the TEM array sensors, which measure the early time response starting at 0.04 msec. The situation is somewhat worse for the BUD sensors, which have only a decade of bandwidth from about 0.15 msec to 1.5 msec. Not only are they incapable of resolving $\tau_M$ for many targets of interest, but they are also incapable of resolving the late stage decay time scale $\tau_0$ for most objects of interest. The design study [29] concluded that the BUD sensors would provide adequate classification performance, but a comprehensive assessment of the added value of

extended bandwidth plus measured on-time response for bulk magnetization has not been performed. Such a study would help establish the limits of UXO/clutter classification performance that can be achieved with EMI sensors.

The main concerns with position error tolerant processing of EMI data are noise and data density or coverage. In our experience processing survey data collected with the EM61, careful leveling of the data is crucial. Different signal offsets in the different time gates will corrupt the decay curves and degrade the classification performance. To ensure complete coverage of all aspects of the target, the measurements should subtend a solid angle of ~1.84 sr at the target, i.e. a cone with 90° apex angle. Roughly speaking, this corresponds to a patch of ground with linear dimensions equal to twice the overall height of the sensor above the target. About three to four dozen measurements spread over a square region like that should provide complete sampling of all of the principal axis responses.

## 9. References


1. George, Vivian and Thomas Altshuler, "Summary of the DARPA Background Clutter Data Collection Experiment," IEEE International Conference on Fuzzy Systems, Anchorage, Alaska, May 4-9, 1998
2. George, Vivian, Thomas W. Altshuler and Erik M. Rosen, "DARPA Background Clutter Data Collection Experiment Excavation Results," Proc. SPIE Conference on Detection and Remediation of Mines and Minelike Targets III, SPIE Vol. 3392, pp. 1000-1011, April 1998.
3. Nelson, Herb, T. Bell, D. Steinhurst and D. George, "EMI Array for Cued UXO Discrimination," The UXO/Countermine/Range Forum 2007 Conference Proceedings, Orlando, Florida, August 28-30, 2007.
4. Nelson, H.H., D.A. Steinhurst, T. Bell and D. George, "EMI Array for Cued UXO Discrimination," Partners in Environmental Technology Technical Symposium, Washington, D.C., December 2-6, 2007.
5. Won, I.J., D.A. Keiswetter, D.R. Hanson, E. Novikova, and T.M. Hall, "GEM-3: A monostatic broadband electromagnetic induction sensor," *J. Environmental and Engineering Geophysics*, vol. 2, no. 1, pp. 53-64, March 1997.
6. Nelson, Herbert H., J.R. McDonald and Richard Robertson, "Design and Construction of the NRL Baseline Ordnance Classification Test Site at Blossom Point," Naval Research Laboratory Report NRL/MR/6110-00-8437, March 20, 2000.
7. Wait, J.R. and K.P. Spies, "Quasi-static Transient Response of a Conducting Permeable Sphere," *Geophysics*, vol. 4, no. 5, pp. 789-792, October 1969.
8. Bozorth , Richard M., *Ferromagnetism*, IEEE Press Classic Reissue, John Wiley & Sons, New Jersey, 2003, Ch. 9.
9. Grant, F. and G. West, *Interpretation Theory in Applied Geophysics*, McGraw-Hill, New York, 1965, §17-2.
10. Landau, L.D. and E.M. Lifschitz, *Electrodynamics of Continuous Media*, Pergammon Press, New York, 1960, §§45, 62.
11. Baum, Carl E., "Low-Frequency Near-Field Magnetic Scattering from Highly, but not Perfectly, Conducting Bodies," Chapter 6, pp. 163-218, in Carl E. Baum (ed.), *Detection and Identification of Visually Obscured Targets*, Taylor and Francis, New York, 1999.
12. Das, Yogadish, John E. McFee, Jack Toews and Gregory C. Stuart, "Analysis of an Electromagnetic Induction Detector for Real-Time Location of Buried Objects," *IEEE Trans. Geoscience and Remote Sensing*, vol. 28, no. 3, pp. 278-288, May 1990.
13. Pasion, Leonard R. and Douglas W. Oldenburg, "A Discrimination Algorithm for UXO Using Time Domain Electromagnetics," *J. Environmental and Engineering Geophysics*, vol. 6, no. 2, pp. 91-102, June 2001.
14. Bell, Thomas H., Bruce J. Barrow and Jonathan T. Miller, "Subsurface Discrimination Using Electromagnetic Induction Sensors," *IEEE Trans. Geoscience and Remote Sensing*, vol. 39, no. 6, pp. 1286-1293, June 2001.
15. Norton, Stephen J., I. J. Won and Ernesto R. Cespedes, "Ordnance/Clutter Discrimination Based on Target Eigenvalue Analysis," *Subsurface Sensing Technologies and Applications*, vol. 2, no. 3, pp. 285-298, July 2001
16. Zhang, Yan, Leslie Collins, Haitao Yu, Carl E. Baum and Lawrence Carin, "Sensing of Unexploded Ordnance With Magnetometer and Induction Data: Theory and Signal Processing," *IEEE Trans. Geoscience and Remote Sensing*, vol. 41, no. 5, pp. 1005-1015, May 2003.

17. Tarokh, Ashley B., Eric L. Miller, I. J. Won and Haoping Huang, "Statistical Classification of Buried Objects from Spatially Sampled Time or Frequency Domain EMI Sensors," *Radio Science*, vol. 39, no. 4, RS4S05, June 2004.
18. Miller, Jonathan T., Thomas H. Bell, Judy Soukup and Dean Keiswetter, "Simple Phenomenological Models for Wideband Frequency Domain Electromagnetic Induction," *IEEE Trans. Geoscience and Remote Sensing*, vol. 39, no. 6, pp. 1294-1298, June 2001.
19. Casey, Kendall F. and Brian A. Baertlein, "An Overview of Electromagnetic Methods in Subsurface Detection," Chapter 2, pp. 9-46 in C. E. Baum (ed.), *Detection and Identification of Visually Obscured Targets*, Taylor and Francis, New York, 1999.
20. Kaufman, Alexander A., *Geophysical Field Theory and Method, Part C: Electromagnetic Fields II*, Academic Press, New York, 1994, §3.III.
21. Weichman, Peter B., "Universal Early-Time Response in High-Contrast Electromagnetic Scattering," *Physical Review Letters*," vol. 91, no. 14, 143908, 3 October 2003.
22. Weichman, Peter B., "Surface Modes and Multipower-Law Structure in the Early-Time Electromagnetic Response of Magnetic Targets," *Physical Review Letters*, vol. 93, no. 2, 023902, 9 July 2004.
23. Bell, Thomas, Bruce Barrow, Jonathan Miller and Dean Keiswetter, "Time and Frequency Domain Electromagnetic Induction Signatures of Unexploded Ordnance," *Subsurface Sensing Technologies and Applications*, vol. 2, no. 3, pp. 153-175, July 2001.
24. Erdelyi, A. (ed.), *Tables of Integral Transforms*, vol. 1, McGraw-Hill, New York, 1954, §5.3, equation (4).
25. Gasperikova, Erika, J. Torquil Smith, H. Frank Morrison and Alex Becker, "Berkeley UXO Discriminator (BUD)," Symposium on the Applications of Geophysics to Environmental and Engineering Problems (SAGEEP), Denver, Colorado, April 1-5, 2007.
26. Moskowitz, R. and E. Della Torre, "Theoretical Aspects of Demagnetization Tensors," *IEEE Trans. Magnetics*, vol. 2, no. 4, pp. 739-744, December 1966.
27. Chen, Du-Xing, James A. Brug and Ronald B. Goldfarb, "Demagnetizing Factors for Cylinders," *IEEE Trans. Magnetics*, vol. 37, no. 4, pp. 3601-3619, July 1991.
28. Stoner, Edmund C., "The Demagnetizing Factors for Ellipsoids," *Philosophical Magazine*, ser. 7, vol. 36, no. 263, pp. 803-821, December 1945.
29. Morrison, Frank, Torquil Smith, Alex Becker and Erika Gasperikova, "Final Report, Detection and Classification of Buried Metallic Objects, UX-1225," Lawrence Berkeley National Laboratory, March 2005.

# Appendix A

## Clutter Items with Slope-Curvature Response Parameters Disjoint from the Corresponding Parameters for Munitions Items

004_in-air.jpg

022_in-air.jpg

029_in-air.jpg

031_in-air.jpg

062_in-air.jpg

071_in-air.jpg

106_in-air.jpg

132_in-air.jpg

145_in-air.jpg

163_in-air.jpg

218_in-air.jpg

224_in-air.jpg

230.jpg

245_in-air.jpg

472_in-air.jpg

481_in-air.jpg

483_in-air.jpg

498.jpg

498_in-air.jpg

568.jpg

616.jpg

650_in-air.jpg

657_in-air.jpg

666_in-air.jpg

671_in-air.jpg

695_in-air.jpg

696.jpg

699.jpg

700_in-air.jpg

733_in-air.jpg

751_in-air.jpg

779_in-air.jpg

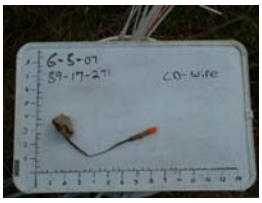

780_in-air.jpg

788.jpg

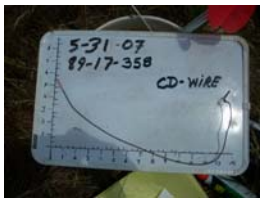

792_in-air.jpg

811_in-air.jpg

814_in-air.jpg

900_in-air.jpg

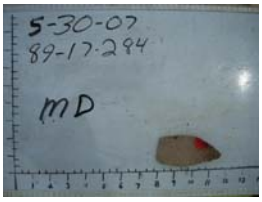

918_in-air.jpg

clutter5.JPG

clutter9.JPG

clutter10.JPG

clutter11.JPG

clutter12.JPG

clutter17.JPG

clutter25.JPG

clutter26.JPG

clutter29.JPG

clutter43.JPG

clutter62.JPG

clutter66.JPG

clutter82.JPG

clutter83.JPG

clutter84.JPG

clutter85.JPG

clutter86.JPG

clutter88.JPG

clutter90.JPG

clutter92.JPG

clutter93.JPG

clutter96.JPG

clutter98.JPG

clutter103.JPG

clutter106.JPG

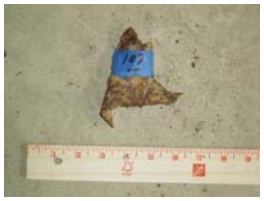
clutter107.JPG

clutter108.JPG

clutter109.JPG

clutter110.JPG

clutter113.JPG

clutter116.JPG

clutter117.JPG

clutter118.JPG

clutter120.JPG

clutter121.JPG

clutter122.JPG

clutter124.JPG

clutter125.JPG

clutter126.JPG

clutter127.JPG

clutter129.JPG

clutter130.JPG

clutter131.JPG

clutter132.JPG

clutter144.JPG

clutter145.JPG

clutter148.JPG

clutter150.JPG

clutter152.JPG

clutter157.JPG

clutter159.JPG

clutter160.JPG

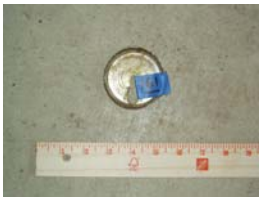
clutter161.JPG

clutter164.JPG

clutter165.JPG

clutter167.JPG

clutter169.JPG

clutter174.JPG

clutter179.JPG

clutter183.JPG

clutter187.JPG

clutter188.JPG

clutter191.JPG

clutter196.JPG

clutter199.JPG

clutter200.JPG

# Appendix B

## Clutter and Munitions Items from Aberdeen Test Site

500 POUND BOMB.jpg

2.75 INCH ROCKET M230.jpg (2)

40MM MKII PROJECTILE.jpg (2)

57MM PROJECTILE APC M86.jpg (3)

81MM M374 PROJECTILE.jpg (2)

105 M60 PROJECTILE.jpg

105mm HEAT ROUND M456.jpg

155MM PROJECTILE M483A1.jpg

CL0770.JPG

CL0861.JPG

CL0871.JPG

CL0873.JPG

CL0874.JPG

CL0881.JPG

CL0886.JPG

CL0919.JPG

CL1228.JPG

CL1256.JPG

CL1284.JPG

CL1402.JPG

CL1744.JPG

CL1884.JPG

CL0755.JPG